ELSEVIER

Contents lists available at ScienceDirect

Computers and Geotechnics

journal homepage: www.elsevier.com/locate/compgeo



Research paper



Fabric anisotropy effects on static liquefaction under constant shear drained loading

Srinivas Vivek Bokkisa^a, Jorge Macedo^{a,*}, Alexandros L. Petalas^b

- a School of Civil and Environmental Engineering, Georgia Institute of Technology, Atlanta, GA, United States
- ^b Department of Engineering, Durham University, Durham, UK

ARTICLE INFO

Keywords: Static liquefaction Anisotropic critical state theory Instability onset Constant Shear Drained (CSD) Fabric anisotropy

ABSTRACT

Several case history failures of slope systems have highlighted that the instability onset in loose materials can be triggered under prevailed drained conditions and stress paths that can be represented by constant shear drained (CSD) loading. This study uses the anisotropic critical state theory (ACST) to assess the effect of fabric anisotropy and loading characteristics (e.g., Lode angle and principal stress direction) on the instability onset under CSD stress paths, comparing our numerical-based observations with available experimental information. Towards this end, the ACST-based SANISAND-F model's performance under CSD stress paths is also assessed. In addition, multiaxial conditions are incorporated through the estimation of instability surfaces. The numerical simulations are useful in explaining that the instability onset under CSD loading is dictated by a trade-off of volumetric strain components. Moreover, the results show an important effect of fabric anisotropy on the instability stress ratio (η_f). For conditions representative of common experimental setups, η_f decreases with the increase of the Lode angle and the major principal stress inclination, and η_f increases with the increase of initial fabric intensity, consistent with available experimental evidence. However, these trends can change based on the interaction between the Lode angle and loading/fabric directions; hence, departing from typical experimental observations. Finally, we discuss the potential of a simplified approach to estimate η_f analytically, including fabric effects.

1. Introduction

Static liquefaction has been associated with several catastrophic failures of slope systems such as tailings storage facilities (TSFs) and water dams, some of them occurring during the last decade (Morgenstern et al., 2016; Jefferies et al., 2019; Robertson et al., 2019; Embankments and Committee, 2021). Static liquefaction can be regarded as an instability type occurring in particulate materials where large plastic strains are developed due to a lack of strength under a given combination of stresses (Chu et al., 2003). It is well established that loose particulate materials can experience static liquefaction when subjected to monotonic shear loading under undrained conditions (Kramer, 1985; Konrad, 1993; Ishihara, 1996; Kramer, 1996). However, several case history failures have also highlighted that static liquefaction can be triggered by prevailing drained loading conditions. For instance, the Wachusett Dam failure in 1907 (Olson, 2000), the Aberfan coal tip disaster in 1966 (Bishop et al., 1969; Jefferies and Been, 2015), the TSF failures at Stava in 1985 (Morgenstern, 2001), Fundao in 2015 (Morgenstern et al., 2016) and Cadia in 2018 (Jefferies et al., 2019), and more recently the failure of the Edenville-Sanford dam in 2020 (Embankments and Committee, 2021; France et al., 2022), are prime examples of static liquefaction where drained conditions prevailed before the instability triggering.

Fig. 1a shows the failure mechanism of the 1907 Wachusett dam failure schematically. According to Olson (2000), a rise of the water table under drained conditions caused a significant decrease in the effective vertical stresses while the shear stress changed only marginally. This change in stresses can be represented by the stress path in Fig. 1b, which can be idealized in the laboratory through a constant shear drained (CSD) test (Brand, 1981; Anderson and Riemer, 1995). A CSD test is commonly conducted in triaxial equipment, considering two stages. First, a standard triaxial loading is imposed until reaching the desired deviatoric loading (q), and then in a second stage, the vertical and confining stresses are released by the same amounts, hence decreasing the mean effective stress (p') under a constant q. Fig. 1 (b,c)schematically shows the typical CSD test response for a loose material where instability can be observed. The instability is associated with a stress ratio ($\eta = q/p'$) on the instability line depicted in Fig. 1b. In addition, large shear strains are developed on further shearing beyond

^{*} Corresponding author.

E-mail address: jmacedo3@gatech.edu (J. Macedo).

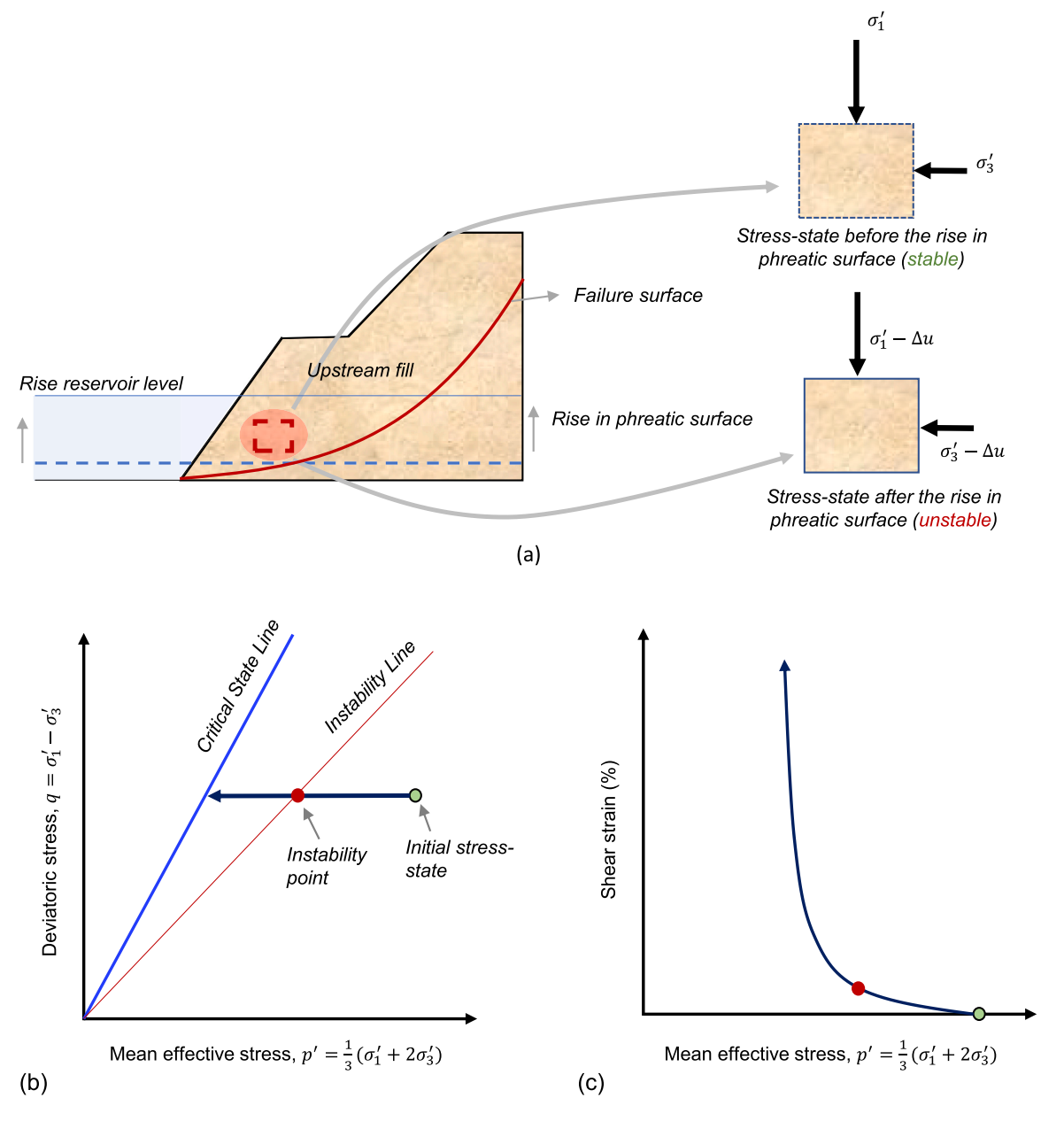


Fig. 1. (a) Illustration of the cross-section through the failed portion of the North Dike of Wachusett Dam highlighting the sliding surface and the stress state at a certain location. (b, c) Schematic of the behavior of loose granular material subjected to CSD loading showing a typical stress path (b) and shear strain versus mean effective stress (c) responses.

the instability point as illustrated in Fig. 1c. Previous research has suggested that instability triggers when the mobilized $\eta=q/p'$ is higher than $\eta_f=(q/p')_f$ (Lade, 1992). Section 2.2 will discuss in detail the conditions for the instability triggering and the definition of the instability stress ratio $(\eta_f=(q/p')_f)$.

As discussed in Fanni et al. (2022), the CSD stress path is particularly important as it is difficult to obviate the possibility of a water table increase during the lifetime of a slope system and because any prefailure indicators (e.g., increase in displacements) would be minimal, making it dangerous in terms of static liquefaction (Sasitharan et al., 1993; Reid et al., 2021b). Several previous experimental studies have explored the onset of instabilities under CSD loadings, with most efforts focused on triaxial (i.e., axisymmetric) conditions, considering a range of densities and stresses (Sasitharan et al., 1993; Skopek et al., 1994; Anderson and Riemer, 1995; Gajo et al., 2000; Chu et al., 2003; Azizi, 2009; Chu et al., 2012, 2015; Dong et al., 2016; Fotovvat et al., 2022; Lindenberg and Koning, 1981; Brand, 1981; Harp et al., 1990; Eckersley, 1990). These studies highlight mechanisms consistent with

those illustrated in Fig. 1(b,c). In some cases, comparisons of the instability triggering under CSD and undrained triaxial loadings have also been explored, highlighting similar η_f regardless of the drainage condition if the initial conditions (i.e., density, consolidation stress) are similar (Chu et al., 2012; Dong et al., 2016; Wanatowski et al., 2010; Fotovvat et al., 2022). Comparatively, experimental efforts considering non-triaxial conditions are scarce. For example, Wanatowski et al. (2010) and Wanatowski and Chu (2012) explored the instability of sands in CSD stress paths under plane-strain conditions. The authors observed experimentally that η_f under plane strain conditions was lower than its counterpart under triaxial conditions. More recently, Fanni et al. (2022) used a hollow cylinder apparatus to explore the effect of fabric (induced and inhered) on the onset of instabilities under drained loadings. Their experimental setup attempted to resemble a CSD stress path. They applied loading with different directions of major principal stress relative to the vertical axis to examine induced fabric anisotropy. In addition, they also tested samples prepared with different reconstitution methods to examine inherent anisotropy. Due to experimental limitations, the loading conditions were limited to two different Lode angles (including the Lode angle in triaxial compression conditions) and two different major principal stress directions. The results highlighted an important effect of both induced and inherent fabric on the instability triggering. Specifically, η_f was lower for the higher Lode angle and the stress orientation that deviates more from the vertical.

Previous efforts have also evaluated the instability onset under CSD stress paths numerically. Most of these efforts have been focused on triaxial conditions, using Hill's criterion (Hill, 1958) combined with a constitutive model to assess instability conditions (Sibille et al., 2007; Sawicki and Świdziński, 2010a; Ramos et al., 2012; Sun, 2013; Alipour and Lashkari, 2018). Hence, the underlying constitutive model significantly influences the observations derived from these efforts. For example, Sibille et al. (2007) and Sawicki and Świdziński (2010a) used constitutive models developed by Darve et al. (1995), and Sawicki and Świdziński (2010b,c); Ramos et al. (2012) and Sun (2013) performed simulations using the Dafalias and Manzari (2004) (DM04) model, and Alipour and Lashkari (2018) used an extended DM04 model developed by Golchin and Lashkari (2014). Due to the nature of the constitutive models employed in previous efforts, fabric anisotropy effects on CSD stress paths have rarely been assessed. We are only aware of the studies by Lashkari et al. (2019) and Wu et al. (2020), which employed fabric-dependent constitutive models and discrete element modeling (DEM) simulations to evaluate instability conditions under CSD loading. Lashkari et al. (2019) modified the constitutive model developed by Yang and Li (2004) to incorporate fabric effects. However, in the context of fabric anisotropy, their study was limited to exploring the effect of initial cross-anisotropic fabrics under triaxial compression loading, concluding that initially cross-anisotropic samples had a higher η_f compared with isotropic counterparts. In another effort, Wu et al. (2020) used DEM and ACST-based numerical simulations to investigate micromechanical features of instability triggering in granular materials under varying drainage conditions imposed on proportional strain and CSD loadings. In this context, one of the main contributions of this study is to assess the effect of induced and inherent fabric anisotropic on the instability onset under CSD stress paths comprehensively. Importantly, our simulations also provide insights for scenarios that are difficult to represent experimentally and have not been assessed in previous efforts due to the challenges of imposing generalized loading conditions considering fabric anisotropy. Towards this end, we use the anisotropic critical state theory (ACST) framework, which is amenable to incorporating fabric effects. In particular, the performance of the ACST-based SANISAND-F model (Petalas et al., 2020) under CSD stress paths is first assessed and then used to evaluate generalized fabric effects. Of note, to the author's best knowledge, the performance of an ACST model under complex CSD stress paths, considering rotated principal stresses and the intermediate stress ratio, is assessed for the first time.

The structure of the paper is as follows: After the introduction in Section 1, Section 2 discusses the SANISAND-F model and the derivation of instability criteria that are dependent on the most general form of fabric anisotropy features for CSD stress paths. We then assess the performance of the SANISAND-F model in estimating the instability conditions under CSD stress paths using selected experimental data of well-characterized sands (Section 3). Next, in Section 4, we numerically simulate several multiaxial CSD stress paths to gain insights into the role of fabric and other state variables besides fabric (e.g., density) and loading characteristics, such as Lode angle and direction of the major principal stress on the onset of instabilities under CSD stress paths. In Section 5, we discuss the practical application of the derived instability criterion and lastly in Section 6, we present the conclusions of our study.

Table 1
Main equations of the SANISAND-F model.

Description	Equation		
Fabric tensor F	$F = F n_F;$ $F = \sqrt{F : F};$ $n_F : n_F = 1;$ $trn_F = 0$	(1)	
FAV A	$A = F : n' = Fn_F : n' = FN$		
ACST conditions	$\eta = \eta_c = (q/p)_c = M(\theta); e = e_c = \hat{e}_c(p); A = A_c = 1$		
DSP ζ	$\zeta = \psi - e_A(A - 1)$		
Elastic moduli	$G = G_0 p_{at} \frac{(2.97 - e)^2}{1 + e} \left(\frac{p}{p_{at}}\right)^{1/2}; \ K = \frac{2(1 + v)}{3(1 - 2v)} G$		
Yield Surface	$f = [(s - p\alpha) : (s - p\alpha)]^{1/2} - \sqrt{\frac{2}{3}} m p$		
Flow rule	$R' = Bn - C\left(n^2 - \frac{1}{3}I\right)$		
	$B = 1 + \frac{3}{2} \frac{1 - c}{c} g(\theta) \cos 3\theta; C = 3\sqrt{\frac{3}{2}} \frac{1 - c}{c} g(\theta)$	(8)	
Dilatancy surface	$\boldsymbol{\alpha}_{\theta}^{d} = \sqrt{\frac{2}{3}} \left[g(\theta) M_{c} exp(n^{d} \zeta) - m \right] \boldsymbol{n}$	(9)	
Bounding surface	$\boldsymbol{\alpha}_{\theta}^{b} = \sqrt{\frac{2}{3}} \left[g(\theta) M_{c} exp(n^{b} < -\zeta >) - m \right] \boldsymbol{n}$	(10)	
Critical state surface	$\alpha_{\theta}^{c} = \sqrt{\frac{2}{3}} \left[g(\theta) M_{c} - m \right] \mathbf{n}$		
Loading direction	$n = \frac{r - \alpha}{\sqrt{2/3}m}$		
Dilatancy	$D = A_0 \left(\boldsymbol{\alpha}_{\theta}^d - \boldsymbol{\alpha} \right) : \boldsymbol{n} = \sqrt{2/3} A_d \left(\boldsymbol{M}_{\theta}^d(\zeta) - \boldsymbol{\beta} \right)$		
Plastic Modulus	$K_p = pH(\alpha_{\theta}^b - \alpha) : n = pH(M_{\theta}^b(\zeta) - \beta)$	(14)	
	$H = \frac{2}{3} \frac{h(e, p, A)}{\langle (\alpha - \alpha_{in}) : n \rangle} = \frac{2}{3} \frac{h(e, p, A)}{\langle \beta - \beta_{in} \rangle}$	(15)	
	$h = G_0 h_1 exp(h_2 A)(e^{-1} - c_h)^2 \left(\frac{p}{p_{at}}\right)^{-1/2}$	(16)	
Fabric evolution	$\dot{F} = \langle L \rangle c_0 exp(A)(\mathbf{n'} - r\mathbf{F})$	(17)	
Strain increment	$\dot{\epsilon} = \dot{\epsilon}^e + \dot{\epsilon}^p = \frac{1}{2G}\dot{s} + \frac{1}{3K}\dot{p}I + \langle L \rangle \left(R' + \frac{1}{3}DI\right)$	(18)	
Stress increment	$\dot{\sigma} = 2G\dot{e} + K\dot{\epsilon}_v I - \langle L \rangle (3GR' + KDI)$	(19)	
Plastic multiplier	$L = \frac{1}{K_p} p\mathbf{n} : d\mathbf{r} = \frac{2G\mathbf{n} : \dot{\mathbf{e}} - K(\mathbf{n} : \mathbf{r})\dot{\mathbf{e}_v}}{K_p + 2G - KD(\mathbf{n} : \mathbf{r})}$	(20)	

2. ACST based instability criteria for CSD loading

2.1. SANISAND-F model formulation

The SANISAND-F constitutive model was recently proposed in Petalas et al. (2020). It is part of the SANISAND family of constitutive models and is a direct extension of the critical state-dependent twosurface plasticity model presented in Manzari and Dafalias (1997) and Dafalias and Manzari (2004). The model is developed within the framework of ACST (Li and Dafalias, 2012), which accounts for the effect of fabric anisotropy on the mechanical behavior of granular soils. More details on the model and the ACST framework can be found in Petalas et al. (2020) and Li and Dafalias (2012), respectively. The governing equations of the SANISAND-F model are summarized in Table 1. One of the main features of the model is that it utilizes a normalized deviatoric fabric tensor F (Equation 1) as an evolving state variable via the evolution law \dot{F} in Equation 17. This allows for the definition of a scalar-valued Fabric Anisotropy Variable (FAV) (Li and Dafalias, 2002), which measures the relative orientation between the loading and the fabric directions (Equation 2). As proposed in Li and Dafalias (2012), the original critical state conditions are enhanced via Equation 3, which implies that at critical state, the fabric orientation is aligned with the loading direction. Similarly, the classical state parameter ψ (Been and Jefferies, 1985) is enhanced by fabric anisotropy via the dilatancy state parameter ζ in Equation 4. The new state parameter determines the dilatancy (D) and plastic modulus (K_n) via Equation 13 and Equation 14 respectively, which influences the constitutive relations in Eqs. 18 and 19. Fig. 2 schematically presents the basic characteristics of the model in the π -plane of the deviatoric stress-ratio space (see Fig. 2's caption for descriptions on the surfaces).

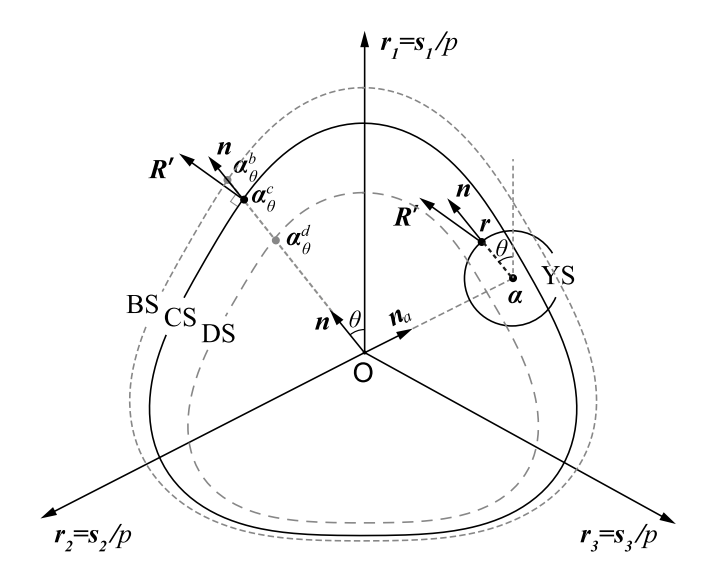


Fig. 2. Illustration of the yield surface (YS), bounding surface (BS), dilatancy surface (DS) and critical surface (CS) on the deviatoric stress ratio space.

Source: From Petalas et al. (2020).

2.2. Instability criteria for CSD stress path incorporating fabric anisotropy

In this section, we first derive instability criteria conditions for CSD stress paths, which are then expressed in terms of the parameters of the SANSISAND-F model. Towards this goal, Hill's instability criterion (Hill, 1958; Rudnicki and Rice, 1975) is used. Hill (1958) postulated that a particulate material is considered stable if the second-order work is positive, i.e., $d^2W = d\sigma' d\varepsilon > 0$. Thus, instability is triggered when $d^2W = 0$, which can be represented by Eq. (21).

$$d\sigma' d\varepsilon = 0 \tag{21}$$

where, σ' and ϵ are the stress and strain tensors, respectively. Substituting, $\sigma'=s+p'I$ and $\epsilon=e+\frac{1}{3}\epsilon_vI$ into the above equation, the instability condition can now be written as:

$$ds: de + \frac{1}{3}dp'd\varepsilon_v = 0 (22)$$

where s is the deviatoric stress tensor and e is the deviatoric strain tensor, p' is the mean effective stress and e_n is the volumetric strain.

In a CSD stress path, the deviatoric stress tensor remains constant, i.e., ds = 0. Hence the instability condition is further simplified to,

$$dp'd\varepsilon_v = 0 \tag{23}$$

Eq. (23) has two possible solutions, $d\varepsilon_v=0$ when $dp'\neq 0$ or dp'=0 when $d\varepsilon_v\neq 0$. These two solutions represent two potential instability types in a CSD stress path. Alipour and Lashkari (2018) defined these instability types as Type 1 and Type 2, as elaborated subsequently.

2.2.1. Type-1 instability criterion

Type-1 instability in a CSD stress path occurs when $d\varepsilon_v=0$, given ds=0 and $dp'\neq 0$. To derive the instability criterion for Type 1 instability in the context of the SANISAND-F model, we start by expressing the total volumetric strain as the sum of its elastic and plastic components, i.e.,

$$d\varepsilon_v = d\varepsilon_v^e + d\varepsilon_v^p \tag{24}$$

The equation above can also be written as,

$$d\varepsilon_v = \frac{dp'}{K} + \langle L \rangle D \tag{25}$$

where K is the bulk modulus, L is the plastic multiplier, D is the dilatancy and $\langle \rangle$ are the Macaulay brackets.

In an elastoplastic loading process, such as the CSD loading, the plastic multiplier L is positive and is given as $L = \frac{1}{K_p} p' n : dr$; hence Eq. (25) can be written as:

$$d\varepsilon_v = \frac{dp'}{K} + \frac{D}{K_p} p' \mathbf{n} : d\mathbf{r}$$
 (26)

The deviatoric stress-ratio is defined as $r = \frac{s}{p'}$, which implies $dr = \frac{ds}{p'} - \frac{rdp'}{p'}$. In a CSD stress path ds = 0. This implies, $dr = -\frac{rdp'}{p'}$. Thus Eq. (26) becomes:

$$d\varepsilon_v = \frac{dp'}{K} - \frac{D}{K_o} dp' \mathbf{n} : \mathbf{r} \tag{27}$$

Type-1 instability occurs when the $d\varepsilon_v = 0$ and $dp' \neq 0$, this implies,

$$K_{n,f} = KDn : r (28)$$

where $K_{p,f}$ is the plastic modulus at the instability point. Hence, the Type-1 instability criterion can be written as $H^1=0$, where

$$H^{1} = K_{p} - K_{p,f} \tag{29}$$

 K_p is the current plastic modulus, which evolves until matches $K_{p,f}$ when instability occurs.

The stress-ratio in multiaxial stress space, i.e., $\beta = \sqrt{3/2}r$: n, at the instability point (β_f) can be derived from Eq. (28) as (Appendix shows the details of the derivation):

$$\beta_f = \frac{-C_1}{3} \left[1 + 2 \left(1 - 3 \frac{C_2}{C_1^2} \right)^{0.5} \cos \left(\frac{\phi + 4\pi}{3} \right) \right]$$

$$\phi = \cos^{-1} \frac{1 + \frac{27C_3}{2C_1^3} - \frac{9C_2}{2C_1^2}}{\left(1 - \frac{3C_2}{C_1^2} \right)}$$
(30)

where $C_1 = -\left(\beta_{in} + M_\theta^d(\zeta)\right)$, $C_2 = -\left(\frac{1}{F_e} - \beta_{in} M_\theta^d(\zeta)\right)$, and $C_3 = \frac{M_\theta^b(\zeta)}{F_e}$. The term F_e in C_2 and C_3 is given as,

$$F_e = \frac{2A_d(1+\nu)(2.97-e)^2}{3(1-2\nu)(1+e)h_1exp(h_2A)(e^{-1}-c_h)^2} \tag{31} \label{eq:fe}$$

This implies that type-1 instability in a CSD loading path occurs when the current stress ratio, i.e., β equals the instability stress ratio, i.e., β_f given according to Eq. (30). Importantly, notice that the terms C_1 , C_2 , C_3 and F_e in Eq. (30) that estimates β_f depend on fabric anisotropy, via the dilatancy state parameter ζ and the fabric anisotropic variable A. This dependence is the critical component that allows us to introduce the effects of fabric anisotropy on the onset of instability in the CSD loading path, as discussed in subsequent sections. Of note, the stress ratio $\eta = q/p'$ in the triaxial space is numerically equal to the stress ratio β in the multiaxial stress space, thus $\eta_f = \beta_f$.

It is worth highlighting that the instability criterion proposed in Bokkisa et al. (2022) for undrained stress paths is consistent with the H^1 instability criterion. This is because the instability conditions in undrained stress paths dictate $d\epsilon_v = 0$, and dq = 0, which incidentally coincides with the conditions for H^1 instability in CSD stress paths.

2.2.2. Type-2 instability criterion

Type 2 instability in a CSD stress path occurs when dp'=0, given ds=0 and $d\epsilon_v\neq 0$. Using these conditions, Eq. (27) can be rearranged as:

$$dp' = 0 = \frac{K_{p,f}K}{K_{p,f} - KD\mathbf{n} : \mathbf{r}} d\varepsilon_v$$
(32)

 $K_{p,f}=0$ is required in Eq. (32) for a non-trivial solution; thus type 2 instability can be expressed as: $H^2=K_p-K_{p,f}=0$.

Since the plastic modulus in SANISAND-F is $K_p = pH(M_\theta^b(\zeta) - \beta)$, the instability stress ratio in the multiaxial stress space for Type 2 instability can be estimated as:

$$\beta_f = M_\theta^b(\zeta) \tag{33}$$

Material parameters of the SANISAND-F model, calibrated for Firoozkuh No. 161 sand and Silica Fine Sand (SFS)

Description	Symbol	Firoozkuh	SFS
Elasticity	G_0	120	120
	υ	0.1	0.05
Critical state	e_{ref}	0.923	0.755
	ξ	0.527	0.27
	λ	0.0569	0.032
	M_c	1.24	1.21
	c	0.8	0.66
Plastic modulus	h_1	12	6
	c_h	0.93	0.9
	n^b	2.5	2.2
Yield surface	m	0.01	0.01
Dilatancy	A_0	0.35	1.2
	n^{d}	7.5	8.0
Fabric	e_A	0.01	0.06
	F_{in}	0.5	0.7
	c_0	1.0	10
	h_2	1.2	1.1
	n_F	$\begin{bmatrix} \frac{2}{\sqrt{6}} & 0 & 0\\ 0 & \frac{-1}{\sqrt{6}} & 0\\ 0 & 0 & \frac{-1}{\sqrt{6}} \end{bmatrix}$	

This implies that Type 2 instability occurs when the mobilized stress ratio is equal to the bounding surface stress ratio, which is dependent on fabric anisotropy via the dilatancy state parameter ζ .

Note that the derived instability criteria in this study share similar functional forms as the criteria derived by Alipour and Lashkari (2018). However, the derivation procedure used in this study is different and, in our opinion, more straightforward as it does not use constitutive matrices. In addition, the criteria derived in this study allow for fabric effects, as already discussed.

3. SANISAND-F performance in simulating CSD stress paths

In this section, we assess the performance of SANISAND-F in simulating CSD stress paths by comparing numerical simulations with selected experimental data produced by Lashkari et al. (2017, 2019) and Fanni et al. (2022) for Firoozkuh No. 161 sand and a silica fine sand respectively. All simulations are performed using the incremental driver code described in Niemunis and Grandas-Tavera (2017) along with a bespoke implementation of the SANISAND-F model to run element tests for various loading paths.

Firoozkuh No. 161 sand is particularly suitable for our purposes as it includes results for triaxial compression/extension and CSD stress paths. Basic properties of the sand include a mean particle size (d_{50}) of 0.276 mm, coefficient of uniformity (C_u) of 1.47, maximum void ratio (e_{max}) of 1.0, and minimum void ratio (e_{max}) of 0.58 (Lashkari et al., 2019). In our assessment, first, the SANISAND-F model parameters are estimated using the triaxial compression/extension data following the calibration protocols in Petalas et al. (2020), and then we use the calibrated SANISAND-F parameters in the simulation of CSD stress paths, comparing the numerical simulations and the available experimental results. The calibrated SANISAND-F parameters for Firoozkuh sand are included in Table 2. Fig. 3(a-f) compares the numerical simulations and the experimental results considering undrained triaxial compression loading conditions for a range of initial densities (i.e., very loose, loose, and medium loose). Fig. 3(g-h) shows similar comparisons considering undrained triaxial extension loading conditions. The numerical simulations are in good agreement with the experimental results, and the model shows good accuracy for various densities and confining pressures for both triaxial compression and extension with the same set of input parameters.

Using the same set of SANISAND-F parameters (Table 2), the CSDstress tests are simulated in 2 stages. First, a conventional triaxial drained loading is imposed until the desired q is reached. Then, the principal stresses are equally relieved, maintaining q constant. Fig. 4 shows the comparison of the SANISAND-F simulated responses and the experimentally observed responses (allowing for uncertainty in e of 0.02 as suggested by Nocilla et al., 2006; Vilhar et al., 2013; Reid et al., 2021a) for a range of initial e (0.844 to 0.948), p' (150 kPa to 350 kPa), and maximum q (110 kPa to 150 kPa) values. Of note, the onset of instabilities in both numerical simulations and experiments are highlighted in Fig. 4. The instability points in the numerical simulation are highlighted based on the previously discussed H^1 and H^2 criteria. In the experiments, the instability point corresponds to the $d\epsilon_v = 0$ condition for loose states, consistently with Hill's criteria. In the case of dense states, the instability is selected when the stress path in the p'-qspace crosses the CSL, as it corresponds to an apparent loss of control in the experiment. The numerical simulations are again in good agreement with the experimental responses (Fig. 4), capturing the experimental patterns for the considered scenarios.

The CSD experimental results in Lashkari et al. (2017) do not consider the effects of loading direction or intermediate stresses; hence, we also considered the experimental results from Fanni et al. (2022), who incorporated these effects. The motivation is to assess the SANISAND-F performance under CSD loading further. Fanni et al. (2022) tested a silica fine sand ($d_{50} = 0.21$ mm, $C_u = 2.3$) in a hollow cylinder, approximating CSD conditions under constant α_{σ} (the relative orientation between the major principal stress axis and the vertical axis) and $b = (\sigma_2 - \sigma_3)/(\sigma_1 - \sigma_3)$ (the intermediate stress ratio). The numerical simulations were conducted for the dry pluviated tests in Fanni et al. (2022) as they include information that allows a better estimation of SANISAND-F parameters (e.g., tests on dense specimens). Most of the SANISAND-F parameters were calibrated following the procedure described in Petalas et al. (2020), except for the fabric-related parameters (e_A, n_d, c_0, h_2) . Due to the unavailability of triaxial extension test data, we modified the approach in Petalas et al. (2020) to calibrate these parameters based on the five undrained hollow cylinder test data available on dense specimens performed at a constant $[\alpha_{\sigma}, b]$ conditions. For instance, consistent with the SANISAND-F equations (see Table 1), we estimate e_A by averaging $\psi^d/(A-1)$ across all undrained hollow cylinder tests, where ψ^d is the state parameter at the phase transformation (PT) point and A is the initial fabric anisotropic variable before undrained shearing. Similarly, we estimate n^d as the average of $\frac{\ln(M^d/M)}{r^d}$ for all undrained tests, where M^d represents the stress-ratio at the PT point, M is the critical state stress-ratio, and ζ^d is determined using Equation 4. We used trial and error for parameters c_0 and h_2 , considering the available test data for different α_{σ} and b. The final parameters are included in Table 2.

Consistent with experiments, the numerical simulations use the octahedral deviatoric stress (q_{oct} - Eq. (34)) and octahedral shear strain (γ_{oct} -Eq. (35)) to represent shear stresses and strains. Moreover, similar to the experiments, the numerical simulations consider two stages. Stage one considers an anisotropic consolidation from an initial isotropic state until the desired target values of q_{act} , p', α_{σ} , and b are reached using constant step increments, and stage two imposes a CSD loading under constant α_{σ} and b.

$$q_{oct} = \frac{1}{\sqrt{2}} \sqrt{(\sigma_{11} - \sigma_{33})^2 + (\sigma_{22} - \sigma_{33})^2 + (\sigma_{11} - \sigma_{22})^2}$$

$$\gamma_{oct} = \frac{2}{3} \sqrt{(\epsilon_{11} - \epsilon_{33})^2 + (\epsilon_{22} - \epsilon_{33})^2 + (\epsilon_{11} - \epsilon_{22})^2}$$
(34)

$$\gamma_{oct} = \frac{2}{3} \sqrt{(\epsilon_{11} - \epsilon_{33})^2 + (\epsilon_{22} - \epsilon_{33})^2 + (\epsilon_{11} - \epsilon_{22})^2}$$
 (35)

Fig. 5 shows the experimental results (Fig. 5 a,c) and the numerical simulations (Fig. 5 b,d) of specimens at similar void ratios after anisotropic consolidation ($e_{in} \approx 0.68$) subjected to undrained shearing at different constant α_{σ} and b stress paths. Consistent with the experiments, the numerical results show that a contractive response is enhanced as α_{σ} or b increases. However, it is important to note that the experimental test conducted with $[\alpha_{\sigma} = 22.5^{\circ}, b = 0.5]$ exhibited a dilative response compared to the test with $[\alpha_{\sigma} = 0^{\circ}, b = 0]$, contrary

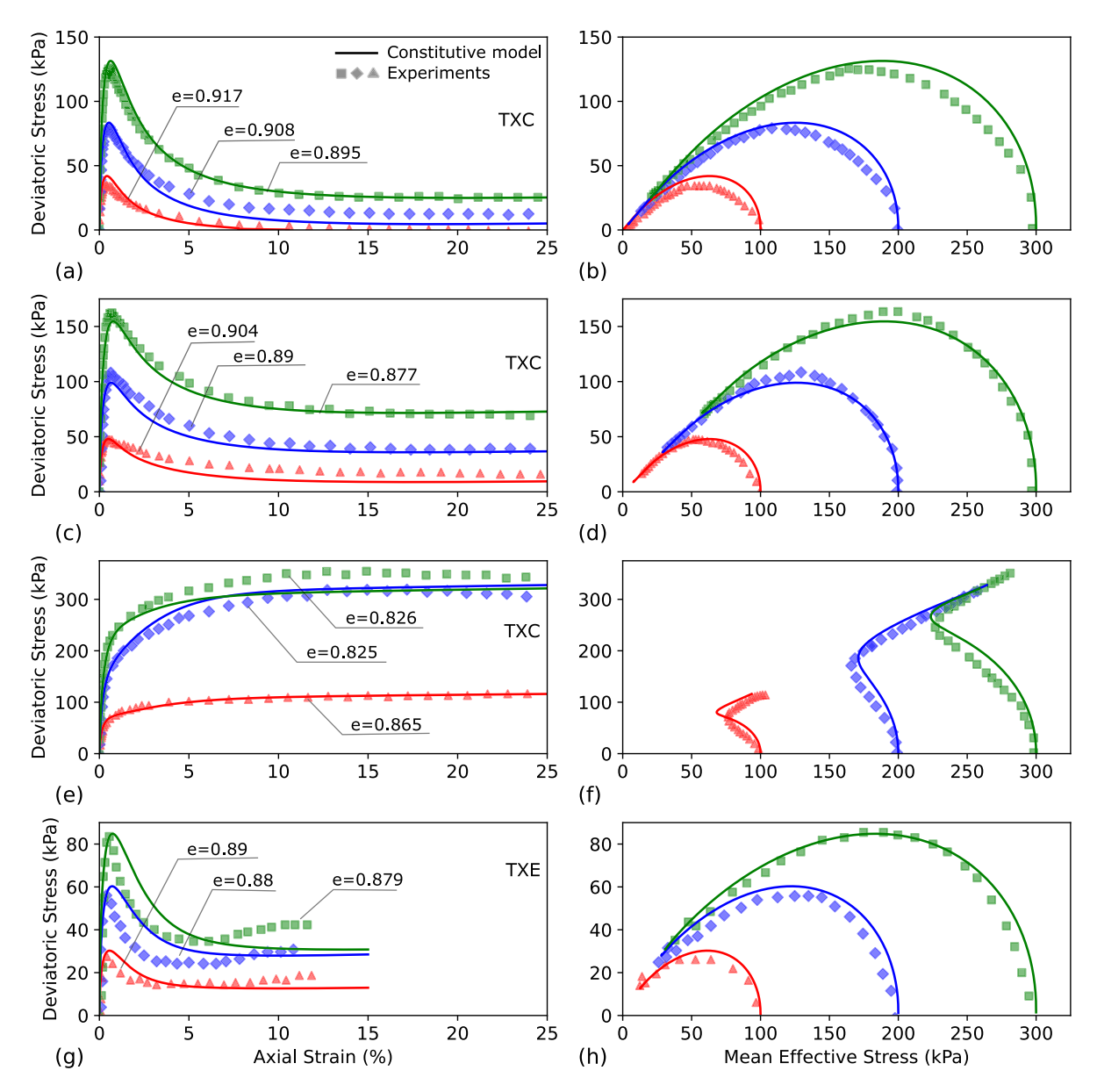


Fig. 3. SANISAND-F model simulations against the experimental data of Firoozkuh No. 161 sand. Figures (a) to (h) show stress-strain and stress paths. (a,b) Triaxial compression test, very loose sand (e = 0.895 - 0.917, p' = 100 - 300 kPa); (c,d) triaxial compression test, loose sand (e = 0.877 - 0.904, p' = 100 - 300 kPa); (e,f) triaxial compression test, medium loose sand (e = 0.825 - 0.865, p' = 100 - 300 kPa); (g,h) triaxial extension test, loose sand (e = 0.879 - 0.89, p' = 100 - 300 kPa).

to the expected trend and prior literature (Yoshimine et al., 1999). Consequently, the numerical simulation fails to capture the behavior of the experiment with [$\alpha_{\sigma}=22.5^{\circ},b=0.5$] but performs reasonably well for all other test conditions. The fact that SANISAND-F can capture this behavior is due to its formulation within the ACST framework. The numerically estimated η_f are also in reasonable agreement compared to experiments. Overall, we find the predicted responses satisfactory and comparable with the SANISAND-F calibration for other sands (e.g., Toyoura sand calibrated in Petalas et al. (2020)).

Using the same set of parameters, the hollow cylinder CSD tests are simulated. Fig. 6 compares numerical simulations and experimental tests, considering CSD loading under different α_{σ} and b and initial void ratios in the range ($e_{in}\approx 0.64-0.70$). The instability onset is also highlighted. The instability points are determined in the numerical simulations based on the H^1 and H^2 criteria discussed earlier. In the experiments that show a transition from volume increase to decrease, the instability point corresponds to the condition of $d\epsilon_v=0$, consistent with Hill's criterion. In the case of continuously dilating specimens, the instability is identified when q_{oct} starts to decrease, indicating a loss of

control during the experiment. Fig. 6(a,b) illustrate the results of CSD tests performed on specimens with similar void ratios ($e_{in} \approx 0.68$) but subjected to different CSD stress paths: $[\alpha_{\sigma} = 0^{\circ}, b = 0], [\alpha_{\sigma} = 22.5^{\circ},$ b=0.2], and [$\alpha_{\sigma}=45^{\circ}$, b=0.2]. The experimental responses show a dilative response throughout the test when $[\alpha_{\sigma} = 0^{\circ}, b = 0]$ and $[\alpha_{\sigma} = 22.5^{\circ}, b = 0.2]$. However, the specimen subjected to $[\alpha_{\sigma} = 45^{\circ},$ b = 0] shows a transition from volume increase to volume decrease (see Fig. 6b). The numerical simulations show a response consistent with the experiments, highlighting the influence of fabric anisotropy. For instance, Fig. 6b, shows the dilatancy state lines (DSLs) at the instability onset for the three simulations. DSL is the locus of dilatancy void ratio e_d where phase transformation happens. In SANISAND-F, e_d is determined as $e_d = e_c + e_A(A - 1)$. At critical state, where A = 1, DSL becomes identical to CSL. When $A \neq 1$, in ACST $\zeta = e - e_d$ plays a role similar to the $\psi = e - e_c$ in the classical critical state theory. Notably, in the $[\alpha_{\sigma} = 0^{\circ}, b = 0]$ and $[\alpha_{\sigma} = 22.5^{\circ}, b = 0.2]$ simulations, the instability point lies below the corresponding DSLs (i.e., ζ < 0) dictating, a "dilative" response and an H^2 instability. The dilative response occurs because η_f is greater than the dilatancy stress

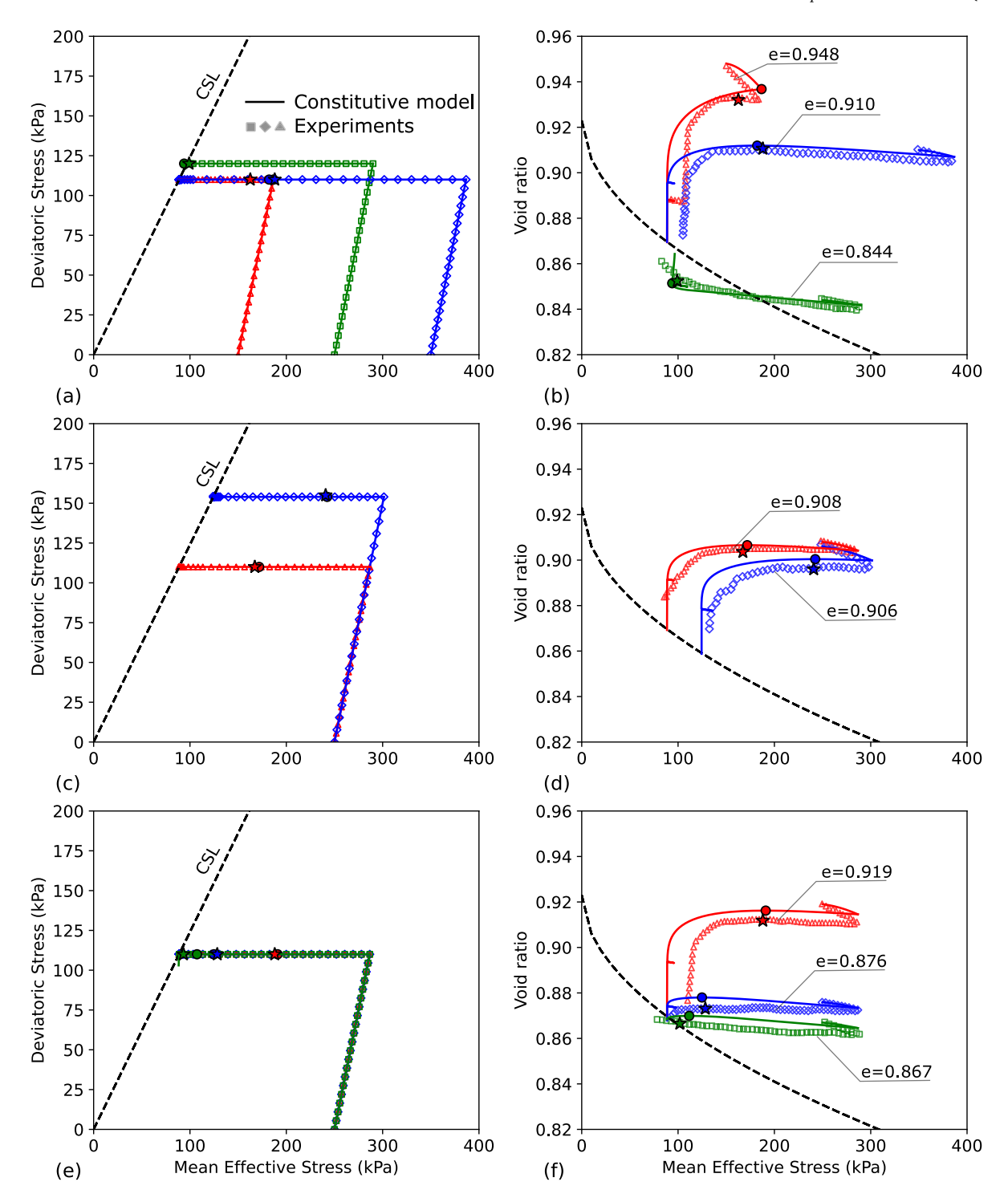


Fig. 4. SANISAND-F constitutive model predictions against the experimental data for Firoozkuh No. 161 sand samples under CSD (stress path, e - p' space). Influence of mean effective stress in (a,b) Influence of constant q in (c,d) Influence of void ratio in (e,f). The marker points represent the instability triggering points in both numerical (\bullet marker) and experimental (\star marker) test results.

ratio, M^d (see Equation 9 and refer Fig. 6a), thus making D<0 (see Equation 13). Conversely, for the $[\alpha_\sigma=45^\circ,\ b=0.2]$ simulation, the instability point lies above the corresponding DSL (i.e., $\zeta>0$), and $M^d>\eta_f$ (refer Fig. 6a) indicating, a "contractive" response (i.e., D>0) and a H^1 instability. Consistent with the ACST framework, the DSL and M^d line location control the dilatancy scaling regardless of the CSL position (above the instability points in all cases). The relative location of the DSL incorporates fabric anisotropic effects, which are key for the numerical simulations being consistent with the experiments. The location of instability points in Fig. 6a are also in good agreement

with the experiments. Fig. 6(c,d) present the results of simulations on specimens with different void ratios ($e_{in}=0.706$ and 0.64) but the same [$\alpha_{\sigma}=45^{\circ}$, and b=0.2]. The experiments show that the specimen with $e_{in}=0.64$ displays a dilative response throughout the test. However, the specimen with $e_{in}=0.706$ transitions from volume increase to decrease as the CSD loading progresses. The numerical simulations capture the combined effects of fabric anisotropy and void ratio on the observed behavior. Similar to the previous simulations, the relative position of the DSL and the M^d line location influence the response at instability. Indeed, the DSL is above the instability point for the simulation, which

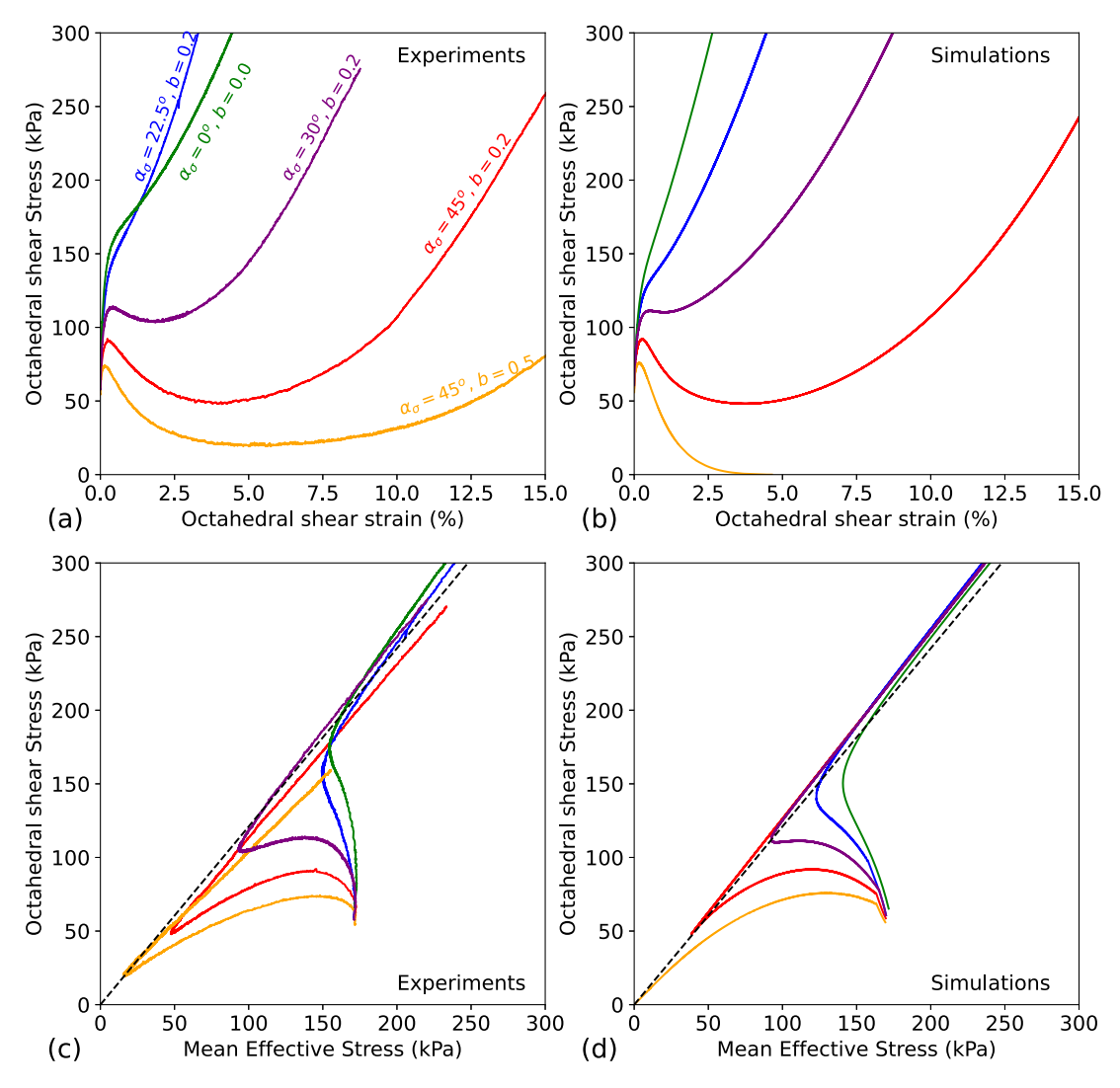


Fig. 5. SANISAND-F model simulations against the experimental data of silica fine sand subjected to undrained loading in a hollow cylinder device. Figures (a) and (c) show stress–strain and stress paths corresponding to the experiments conducted at a similar void ratio (≈ 0.68) but different constant α_{σ} and b conditions. Figures (b) and (d) show the model simulations run under similar conditions as in experiments.

shows a dilative response, and below for the simulation showing a transition in the volume change tendency.

Overall, it can be observed that the CSD loading numerical simulations and experimental results match reasonably well for the examined sands, including cases where α_σ and b vary. Last, Fig. 7 compares the η_f values estimated by SANISAND-F and their experimental counterparts. When the numerically computed η_f matches the experimental estimate, a data point lies on the highlighted x=y line. Again, the SANISAND-F performance in estimating η_f , which is the focus of this study, is satisfactory for CSD stress paths. Of note, the instability stress ratios corresponding to undrained stress paths were estimated numerically following the instability criterion proposed in Bokkisa et al. (2022) and experimentally by capturing the peak point of the soil response in the $p'-q_{oct}$ space.

4. Role of fabric anisotropy on the instability onset under CSD stress paths

This section assesses the role of fabric anisotropy and other state variables on the instability onset under CSD stress paths. We investigate the aforementioned effects by numerically simulating CSD stress paths with anisotropic effects. When experimental observations are available (scarce for CSD stress paths, as discussed in Section 1), we compare the

insights of our simulations against experimental counterparts. Specifically, our simulations consider varying the initial density (illustrating typical instability patterns), the Lode angle (θ) of the principal stress tensor, the rotation of the principal stress axis (α_{σ}) , and the initial fabric intensity (F_{in}) . If the principal stresses are ordered as $\sigma_{11} > \sigma_{22} > \sigma_{33}$, the Lode angle can be estimated as $\theta = \frac{\pi}{6} + tan^{-1}\left(\frac{2b-1}{\sqrt{3}}\right)$. We consider the Firoozkuh sand calibrated parameters as our analyses are focused on investigating general trends.

Previous efforts (Wanatowski, 2005; Fanni et al., 2022) have suggested that stresses typically developing below slopes involved in case history failures (e.g., Fig. 1) may have been likely associated with α_{σ} values between 15° and 45° and b values between 0.2 and 0.5 and initially loose materials (i.e., the initial state in the e-p' space above the CSL); hence, our analyses are focused on these ranges. However, we also explore broader ranges of b and α_{σ} by deriving instability surfaces in the π -plane, following the approaches in Bokkisa et al. (2022). The simulation of CSD stress paths considers an initial stage to reach the targeted q_{oct} , which for convenience is conducted under a constant p', then, a stress relief stage where p' is decreased under a constant q_{oct} . Of note, for a given loading path α_{σ} and θ are maintained constant throughout the simulation of the CSD loading, and the onset of instability is assessed using the criteria previously discussed

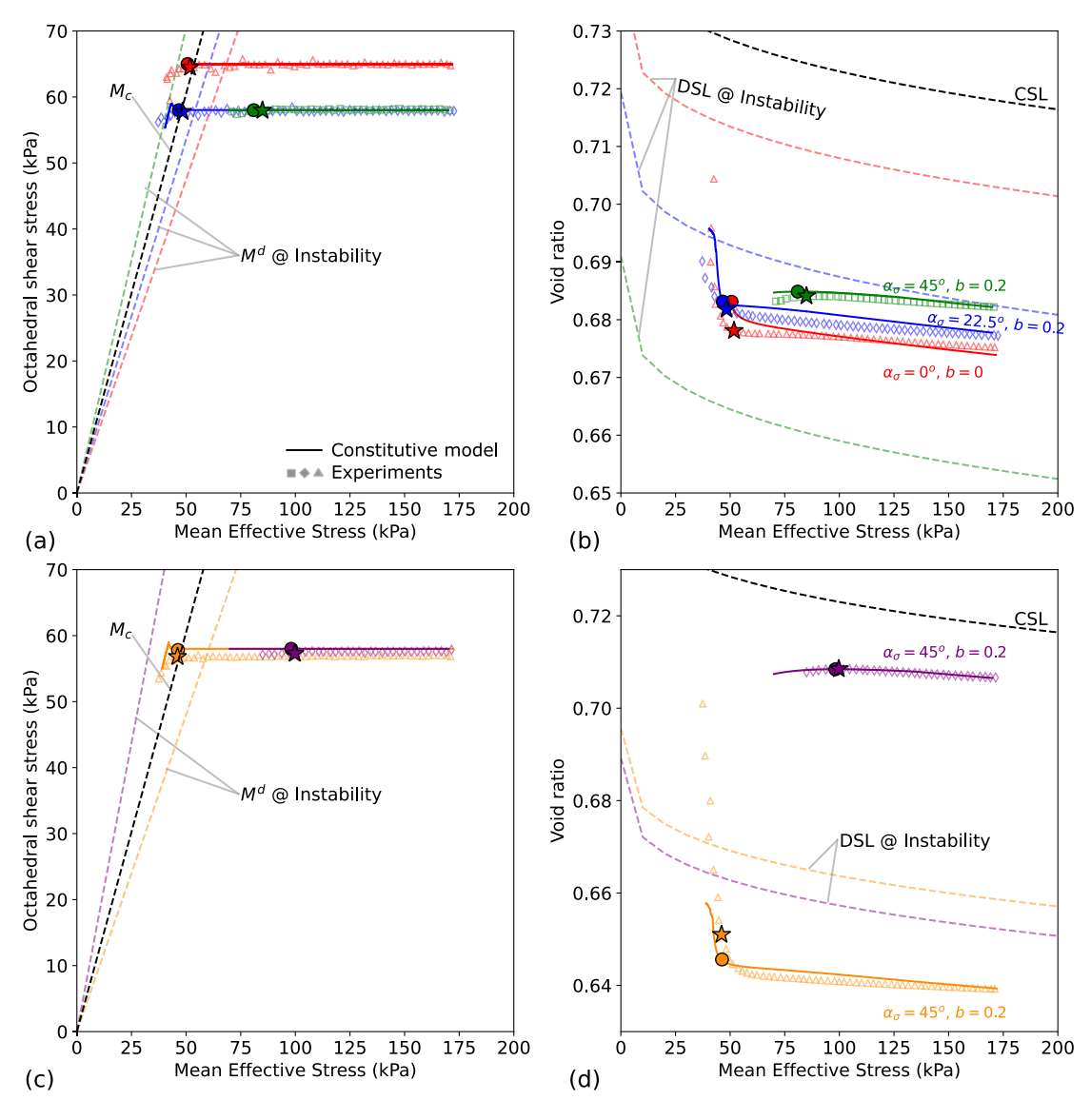


Fig. 6. SANISAND-F constitutive model predictions against the experimental data for silica fine sand samples under CSD (stress path, e-p' space). Influence of fabric anisotropy in (a,b) Influence of void ratio in (c,d). The marker points represent the instability triggering points in both numerical (\bullet marker) and experimental (\star marker) test results. Highlighted DSLs at the instability in e-p' space and dilatancy stress ratios (M^d) at the instability in the $p'-q_{oct}$ space.

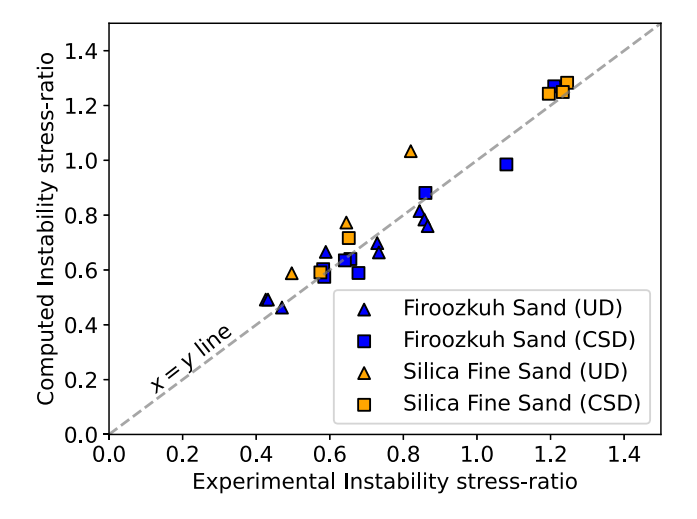


Fig. 7. Comparison of experimental instability stress-ratio against the computed instability stress ratio for the CSD and undrained (UD) tests of Firoozkuh No. 161 sand and the Silica Fine Sand.

(Section 2.2). q_{oct} and γ_{oct} are calculated using Eqs. (34) and (35), unless stated differently.

4.1. Initial density effect and typical Type 1 and Type 2 instability responses

Fig. 8 shows typical responses of CSD stress paths, considering $\alpha_{\sigma}=0^{\circ},\ \theta=0^{\circ}$ (the effect of varying α_{σ} and θ is assessed in the following subsections), $e_{in}=[0.8,0.9,0.95]$, and $p'_{in}=200$ kPa. In the initially loose states (i.e., $e_{in}=0.9$ and 0.95), a Type 1 instability can be observed, where $\eta_{f}=q_{oct}/p'$ is significantly lower than M_{c} (see Fig. 8a), the initial response on the CSD stress relief stage shows a slight increase in void ratio, which is then reverted (see Fig. 8b). After the instability onset, strains are also accelerated (see Fig. 8c) consistently with the numerical results of Alipour and Lashkari (2018). In terms of the variables that track instability conditions, H^{1} becomes zero at a relatively low deviatoric strain; however, H^{2} monotonically decreases but never reaches a zero value. For the initially dense samples ($e_{in}=0.8$), an instability Type 2 can be observed where η_{f} is higher than M_{c} (see Fig. 8a), the response on the CSD stress relief stage is dilative (see Fig. 8b) before and after the instability onset where strains are also accelerated (see Fig. 8c). In this case, H^{2} reaches a zero

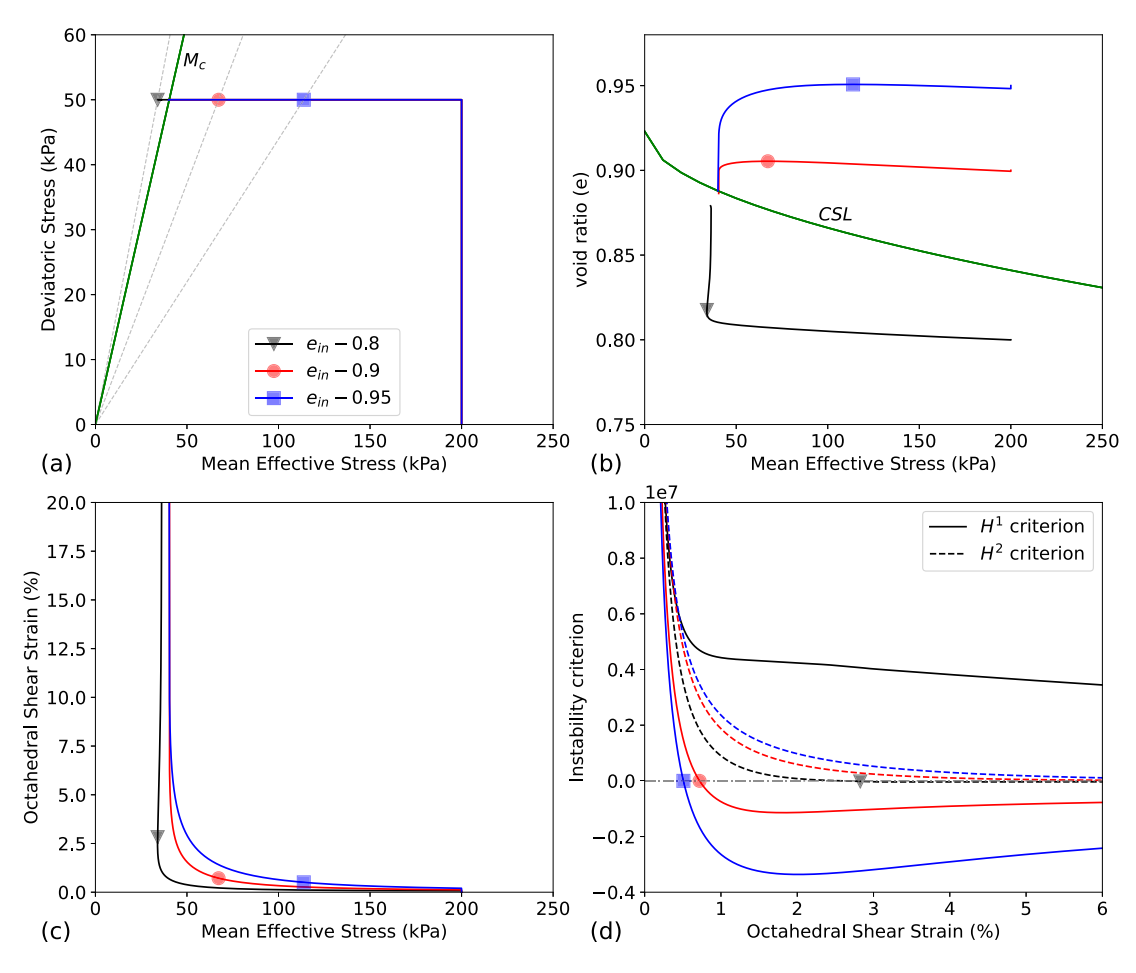


Fig. 8. SANISAND-F constitutive model responses for Firozkuh No. 161 sand specimen at p' = 200 kPa subjected to CSD loading path in triaxial compression conditions for different initial void ratios $e_{in} = [0.8, 0.9, 0.95]$ (a) Stress path (b) e - p' space (c) Octahedral shear strain Vs mean effective stress (d) Evolution of instability criterion with respect to shear strain. The marker points represent the instability triggering points.

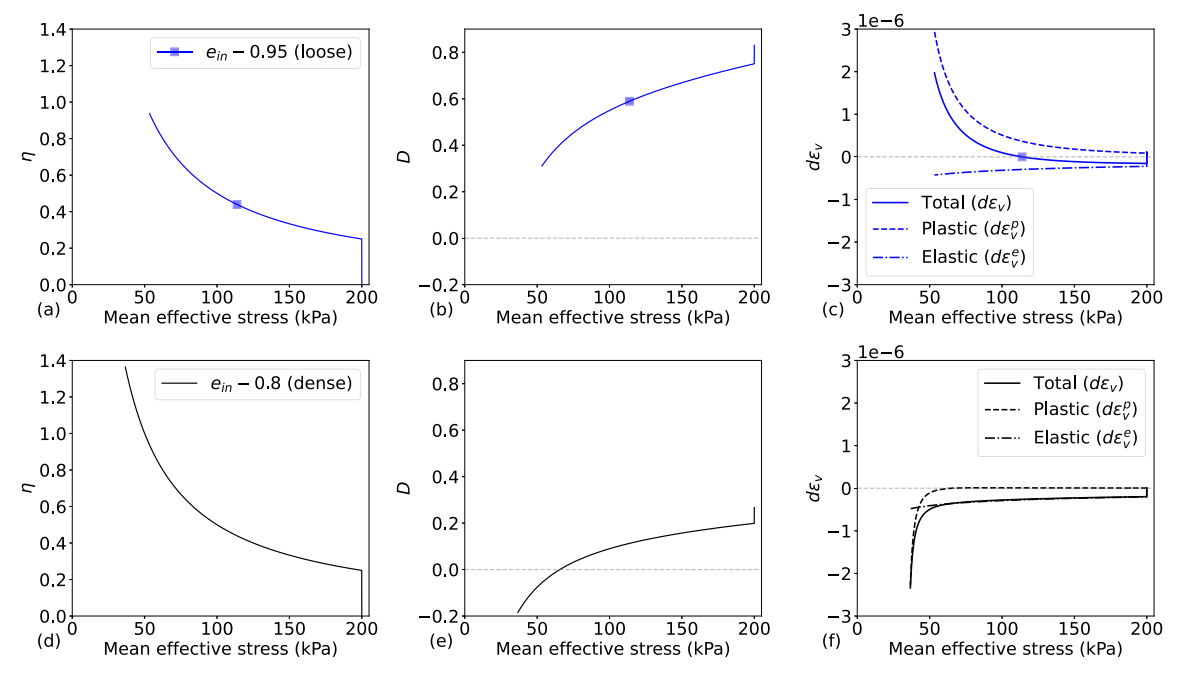


Fig. 9. Evolution of stress-ratio, dilatancy, and volumetric strain increment against mean effective stress for loose sample in (a,b,c) and dense sample in (d,e,f) respectively. The marker points represent the instability triggering points.

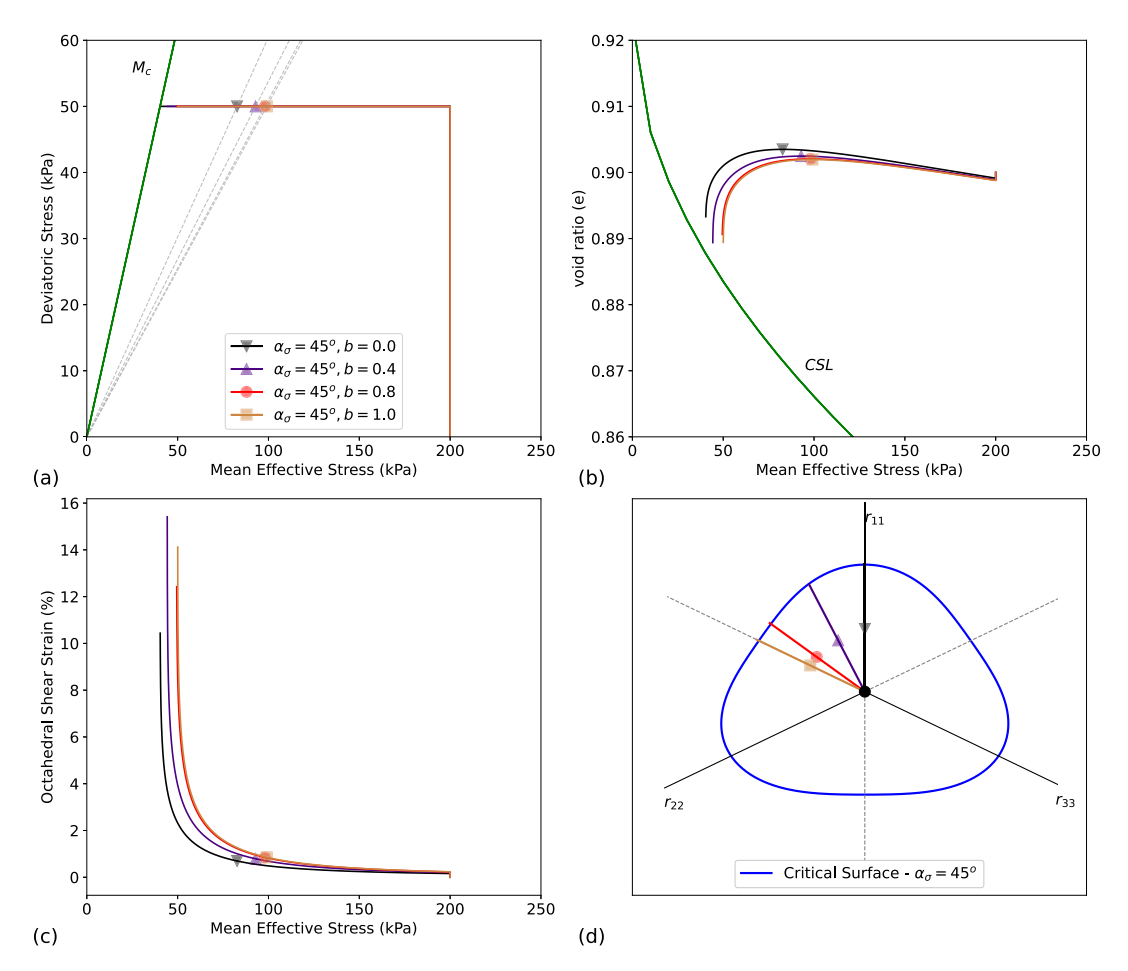


Fig. 10. SANISAND-F constitutive model responses for Firozckuh No. 161 sand specimen at $e_{in}=0.90$ and p'=200 kPa subjected to CSD loading path with $\alpha_{\sigma}=45^{\circ}$ and b=[0,0.4,0.8,1.0]. (a) Stress path (b) e-p' space (c) Octahedral shear strain versus mean effective stress (d) Stress paths represented in the π -plane of the principal deviatoric stress-ratio space corresponding to $\alpha_{\sigma}=45^{\circ}$. The marker points represent the instability points.

value at relatively low strains, consistently with a Type 2 instability; H^1 decreases monotonically; however, without reaching a zero value (Fig. 8d). The aforementioned patterns are consistent with Alipour and Lashkari (2018); however, the derivations in this study enable a comprehensive assessment of fabric effects, as discussed in the next subsections. Last, as expected, η_f increases as e_{in} decreases, which is consistent with previous experimental and numerical studies (Chu et al., 2015; Fanni et al., 2022; Fotovvat et al., 2022; Azizi et al., 2009; Wanatowski et al., 2010; Alipour and Lashkari, 2018; Wu et al., 2020).

Inspecting the volumetric response in CSD stress path allows for a better understanding of the mechanisms at the instability onset. This is illustrated in Fig. 9, which shows the typical evolution of the η , D, and volumetric strain increments for the simulations with $e_{in} = 0.95$ (loose state) and $e_{in} = 0.8$ (dense state) in Fig. 8. The evolutions are shown in terms of p' so readers can inspect Fig. 9 in the context of Fig. 8. First, it is worth noting that η is always increasing; hence the CSD path imposes a continuous loading despite the stress-relief stage, as shown in Fig. 9a. It is also interesting to see that *D* is always positive on initially loose samples, which may suggest a continuous decrease in volume. However, D is only based on plastic strains, and there is also a contribution from elastic strains to the total volumetric strains. To put this into context, note the evolution of elastic $(d\varepsilon^e)$ and plastic volumetric strain $(d\varepsilon_v^p)$ increments in Fig. 9c and how this evolution translates in the rate of total volumetric strain increments ($d\varepsilon_v$ = $d\varepsilon_{v}^{p} + d\varepsilon_{v}^{e}$). In the initial part of the stress relief stage, $d\varepsilon_{v}^{e}$ is negative and $d\varepsilon_v^p$ positive, with the $d\varepsilon_v^e$ magnitude being higher, making $d\varepsilon_v$ negative. As the stress relief progresses, $d\varepsilon_v^p$ becomes more positive, and

eventually, $d\varepsilon_v$ is zero, marking the instability onset and a transition from volume increase to volume decrease. Therefore, the instability triggering is dictated by the trade-off between $d\varepsilon_v^P$ and $d\varepsilon_v^e$. This is an important aspect to highlight in interpreting the mechanisms at the instability onset under CSD loading, yet not pointed out in previous efforts as far as we are aware. In the case of initially dense states, $d\varepsilon_v$ is always negative in the stress relief stage, with $d\varepsilon_v^e$ and $d\varepsilon_v^P$ being also negative. Hence, the instability onset is associated with reaching bounding conditions (i.e., Eq. (33)) without trade-off on volumetric strain components.

4.2. Effect of Lode angle θ (or intermediate stress ratio b)

Fig. 10 shows the simulations of CSD paths considering $\alpha_{\sigma}=45^{\circ}$, $e_{in}=0.9$, $p'_{in}=200$ kPa, a targeted q_{oct} of 50 kPa, and different Lode angles, $\theta=[0^{\circ},23.4^{\circ},49.1^{\circ},60^{\circ}]$ (corresponding to b=[0,0.4,0.8,1.0]). η_f is estimated using the H^1 criterion and highlighted with different markers on each loading path. Fig. 10 also shows the M_c line representing the critical state stress ratio for b=0 for reference. Note that, in general, the critical state stress ratio is Lode angle dependent. It can be observed in Fig. 10a that as b increases, η_f decreases. Fig. 10b shows that instability occurs at the transition between volume increase and decrease responses, consistently with the loose initial state. After the instability onset, the octahedral shear strains also start to increase significantly, as illustrated by Fig. 10c. Last, Fig. 10d shows the stress paths in the π -plane, where differences in the loading path that cannot be appreciated in the p'-q space are now evident. As b is constant,

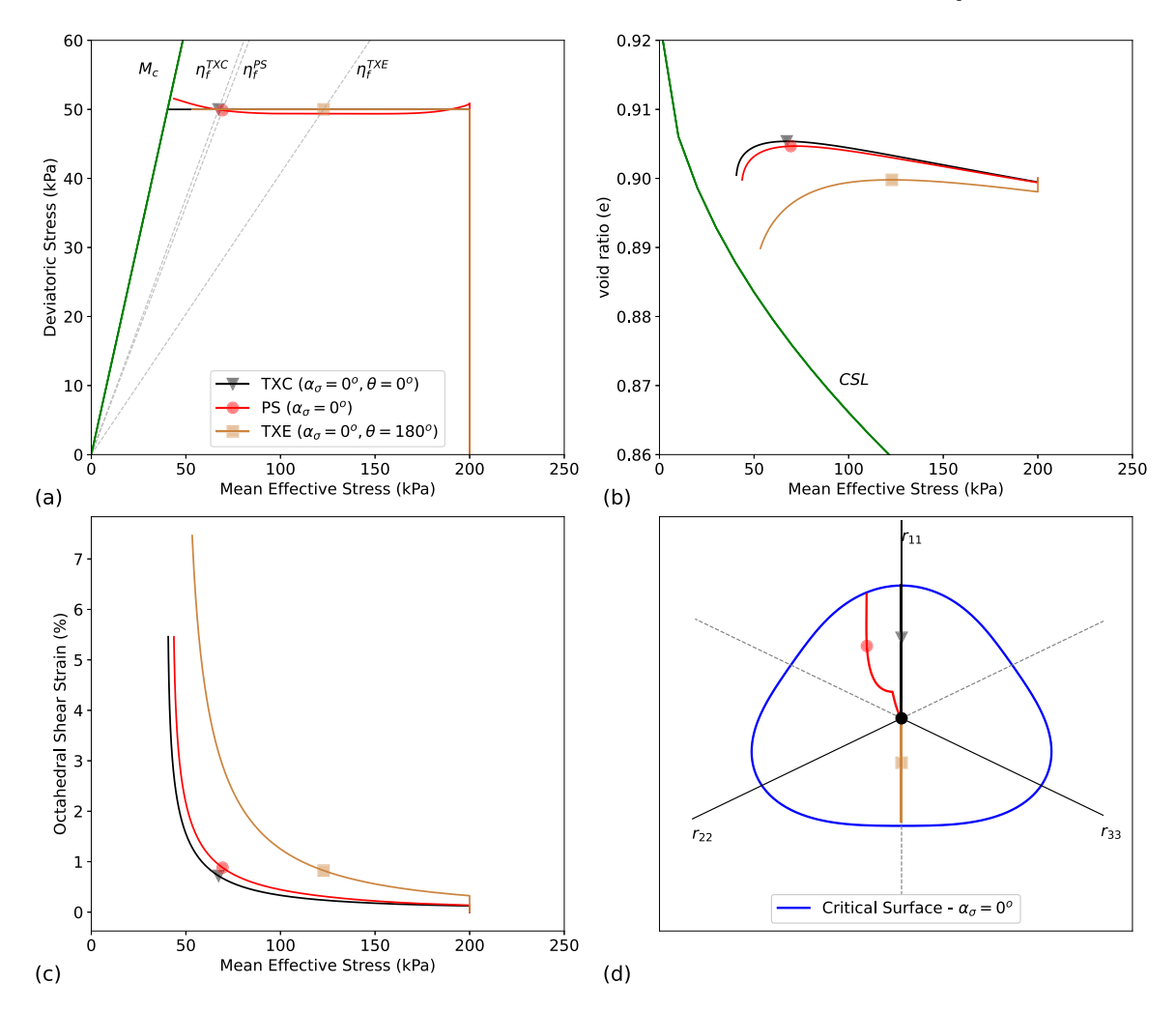


Fig. 11. SANISAND-F constitutive model responses for Firoozkuh No. 161 sand specimen at $e_{in} = 0.90$ and p' = 200 kPa subjected to CSD loading path in triaxial compression, plane strain and triaxial extension conditions. (a) Stress path (b) e - p' space (c) Octahedral shear strain Vs mean effective stress (d) Stress paths represented in the *π*-plane of the principal deviatoric stress-ratio space corresponding to $\alpha_{\pi} = 0^{\circ}$. The marker points represent the instability points.

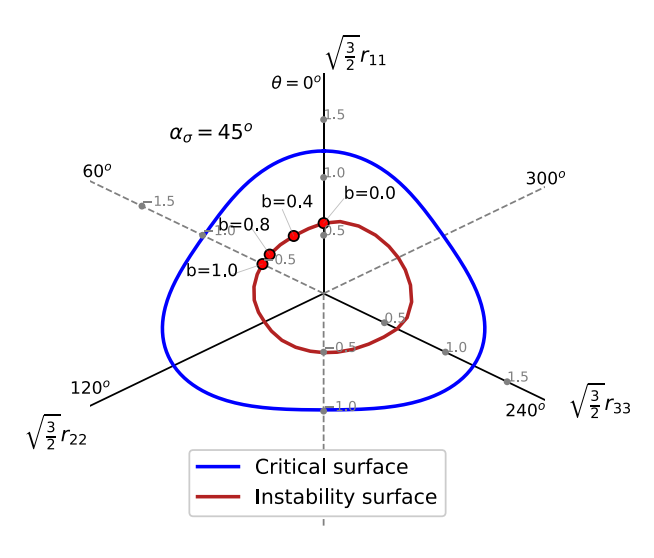


Fig. 12. Instability surface obtained from the numerical simulations of a hollow cylinder test with constant Lode angle (θ) and constant stress principal axis rotation $(\alpha_{\sigma}=45^{\circ})$ using Firoozkuh No. 161 sand properties with $e_{in}=0.9$ and p'=200 kPa. Instability points corresponding to b=[0,0.4,0.8,1.0] are also highlighted.

the stress paths in the π -plane are straight lines. In terms of previous efforts assessing the role of b on η_f under CSD stress paths, we are only aware of the experimental study of Wanatowski et al. (2010), who compared η_f for triaxial paths (i.e., $\alpha_\sigma=0^\circ,b=0$) and plane strain conditions, observing larger η_f in triaxial conditions. Even though b was not estimated by Wanatowski et al. (2010), previous studies have suggested b varying in the range between 0.25 and 0.5 (Sayao and Vaid, 1996; Yoshimine et al., 1999; Shibuya, 1985; Pradhan et al., 1988) for plane strain conditions. Thus, the experimental observations by Wanatowski et al. (2010) are, in general, consistent with the trends in Fig. 10.

Recognizing that triaxial compression, triaxial extension, and plane strain (variable θ or b) conditions are of interest in the assessment of slope systems (Sadrekarimi, 2014; Wanatowski and Chu, 2007), we have assessed CSD stress paths, considering these loading paths. Fig. 11 shows simulations of CSD loading under triaxial compression ($\alpha_{\sigma} = 0^{\circ}$ and $\theta=0^{\circ}$), plane strain ($\alpha_{\sigma}=0^{\circ}$) and triaxial extension conditions $(\alpha_{\sigma} = 0^{\circ} \text{ and } \theta = 180^{\circ})$. Note that in a plane strain condition, the radial strain is constrained, i.e., $\varepsilon_r = \varepsilon_{22} = 0$, but σ_{22} cannot be controlled; thus, q_{oct} cannot be maintained constant (see Eq. (34)) when plane strain conditions are enforced. Hence we simulated a constant $q_{13} = \sigma_{11} - \sigma_{33}$ path with q_{13} maintained constant at 57 kPa, which, in turn, simulates approximately a constant q_{oct} of 50 kPa. This approach is consistent with the strategy used in the experimental study of Fanni et al. (2022). The H^1 instability criterion is still used to estimate η_f under plane strain as q_{oct} is almost constant (see Fig. 11a). Fig. 11 shows that η_f in triaxial compression is higher than η_f in plane strain,

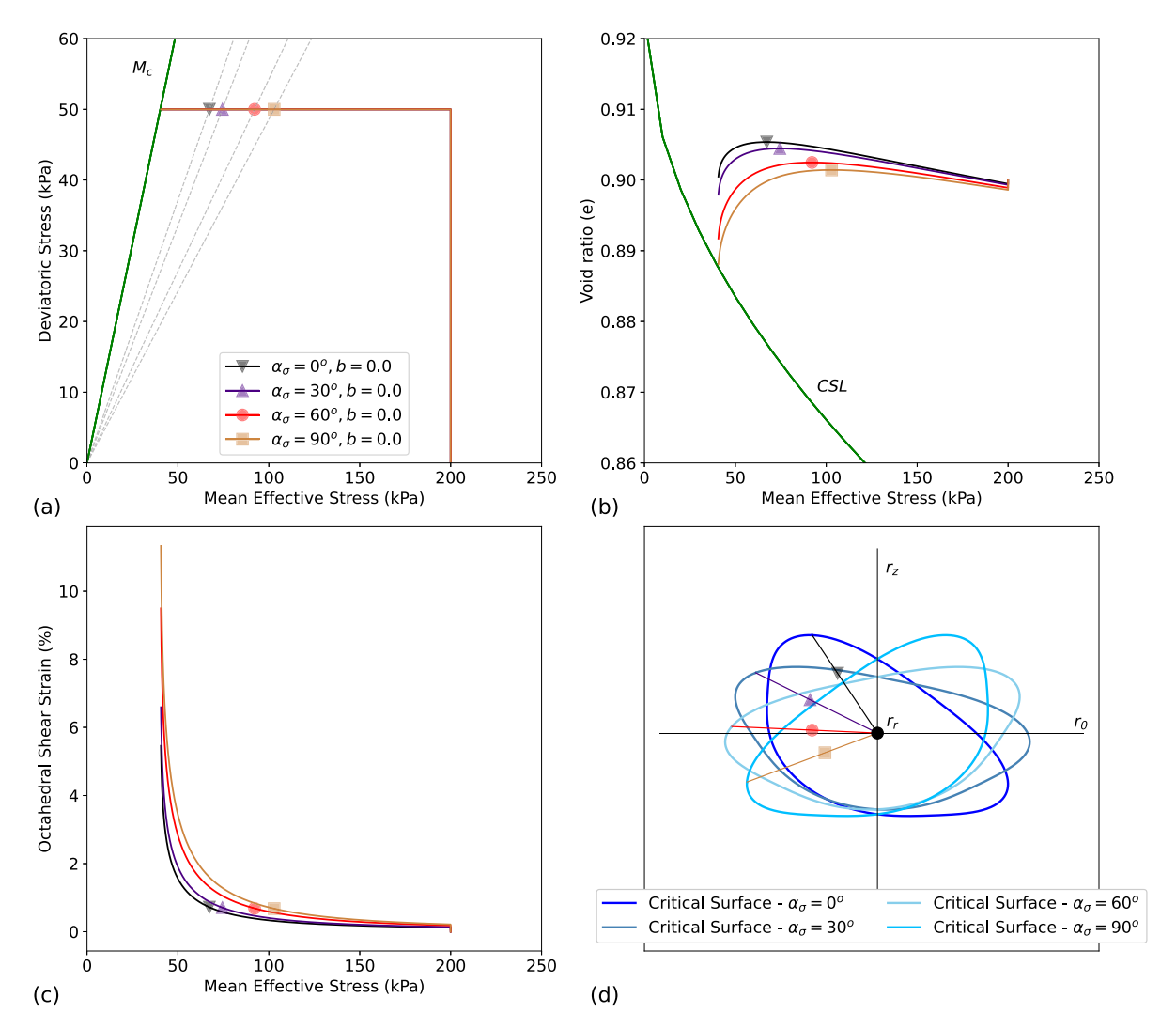


Fig. 13. SANISAND-F constitutive model responses for Firozkuh No. 161 sand specimen at $e_{in}=0.90$ and p'=200 kPa subjected to CSD loading path with $\theta=0^\circ$ (b=0) and $\alpha_\sigma=[0,30^\circ,60^\circ,90^\circ]$. (a) Stress path (b) e-p' space (c) Octahedral shear strain Vs mean effective stress (d) Stress paths represented in the 3D global deviatoric stress-ratio space $(r_z-r_r-r_\theta)$ and viewed through the axis r_r . The marker points represent the instability points.

which in turn, is significantly higher than η_f in triaxial extension. These trends are consistent with the experimental studies by Wanatowski et al. (2010) and Dong et al. (2016). The instability for the three cases occurs at the transition between volume increase and decrease responses during the stress relief (Fig. 11b). After the instability, as the CSD loading progresses, larger strains are developed (Fig. 11c). Fig. 11d shows the stress paths in the π -plane, which enables appreciating the differences between the imposed loading conditions that cannot be properly assessed in the p'-q space. A perfect line in the π -plane implies a constant b value; hence, it can be noticed that for the plane strain case, b is not constant, varying between 0.24 - 0.52 for the conducted simulation. To illustrate the assessment of a broader range of b values, we conducted additional simulations considering $\alpha_{\sigma} = 45^{\circ}$ and varying θ from 0° to 360°. The η_f estimated at instability for these simulations can be plotted in the π -plane of the principal deviatoric stress-ratio space to construct an instability surface. Fig. 12 shows such a surface, where the axes in the π -plane are adjusted to have the distance from the origin to the instability surface also representing η_f in the p'-qspace. Fig. 12 also highlights the instability points corresponding to b =[0, 0.4, 0.8, 1.0]. The interpretation of the instability surface in Fig. 12 is that it separates stable from unstable states for any Lode angle; hence, it provides a full assessment of η_f .

4.3. Effect of loading direction, α_{σ}

Fig. 13 shows the simulations of CSD paths considering $\theta = 0^{\circ}$ (b=0.0), $e_{in}=0.9$, $p'_{in}=200$ kPa, a targeted q_{oct} of 50 kPa, and $\alpha_{\sigma}=[0^{\circ},30^{\circ},60^{\circ},90^{\circ}]$. The η_f estimated using the H^1 criterion are also highlighted. It can be observed that α_{σ} significantly affects the instability triggering and η_f . Indeed, η_f decreases as α_σ increases (see Fig. 13a). Fig. 13b shows that the increase in volume before the instability is less as α_{σ} increases, and Fig. 13c shows that strains increase significantly as the CSD loading progresses after the instability, consistently with previous observations. The difference in the stress paths with respect to α_{σ} can be better distinguished in Fig. 13d where the stress paths are plotted in the global deviatoric stress-ratio space, i.e., $r_z - r_r - r_\theta$ and viewed along the r_r axis. It can be observed as the α_{σ} increases, the stress paths rotate more with respect to the vertical (i.e., r_z axis). In terms of previous studies exploring the effects of α_{σ} under CSD loading, we are only aware of the experimental study by Fanni et al. (2022), who considered α_{σ} values of 22.5° and 45°. The aforementioned trends are consistent with the observations by Fanni et al. (2022) (i.e., η_f decreases as α_{σ} increases). Fig. 14 shows the instability surfaces for different α_{σ} values, considering the full range of θ values. It is interesting to see how the shapes of instability surfaces change as α_{σ} varies, affecting interactions with different Lode angles. For example, for low Lode angles, i.e., $\theta = 0^{\circ}$ to 60° , η_f decreases S.V. Bokkisa et al.

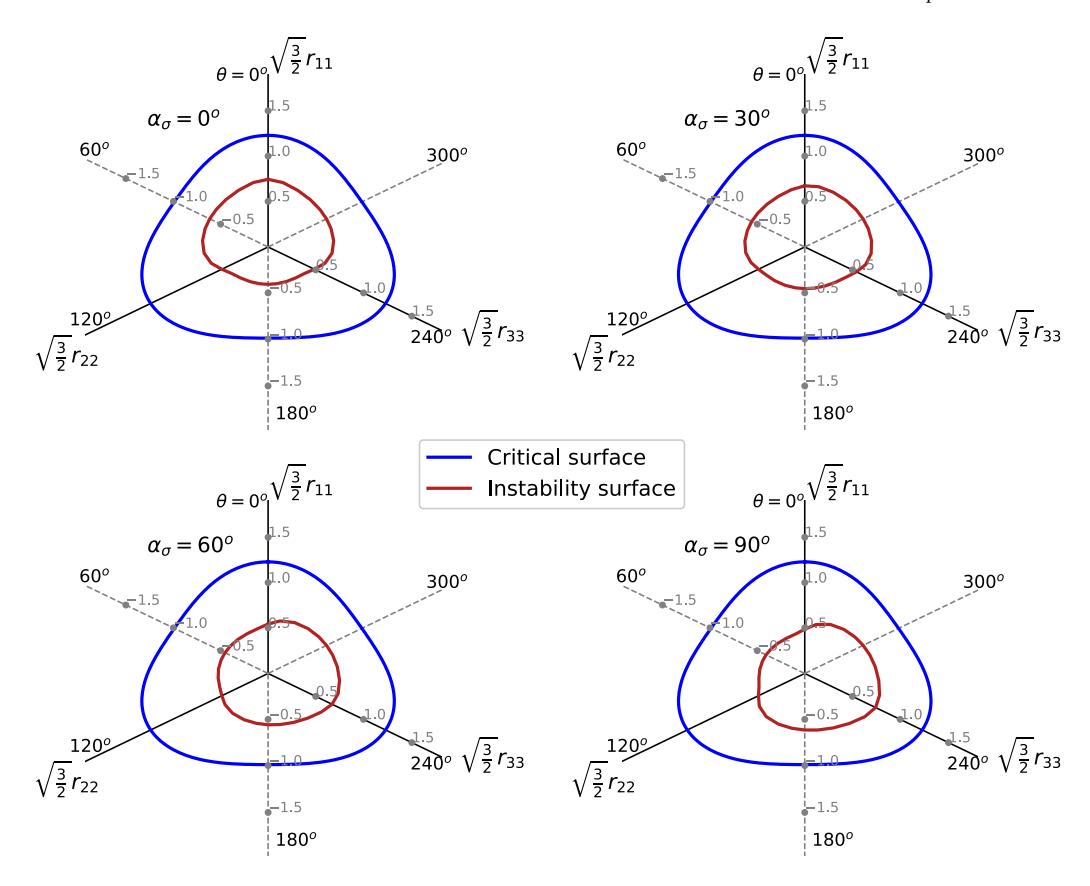


Fig. 14. Instability surface obtained from the numerical simulations of a hollow cylinder test with constant Lode angle (θ) and constant stress principal axis rotation $(\alpha_{\sigma} = [0^{\circ}, 30^{\circ}, 60^{\circ}, 90^{\circ}])$ using Firoozkuh No. 161 sand properties with $e_{in} = 0.9$ and p' = 200 kPa.

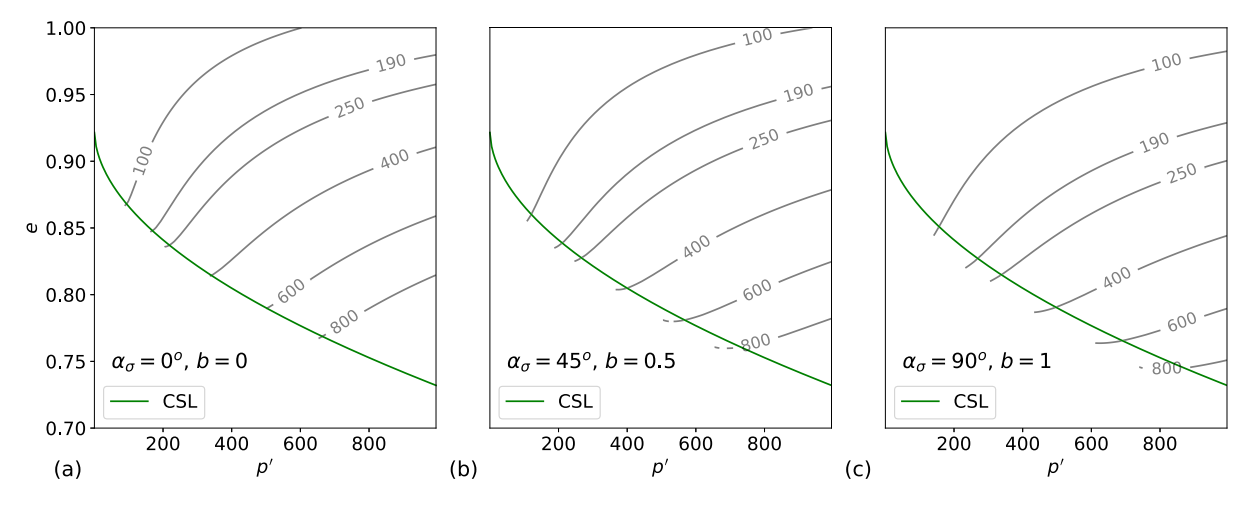


Fig. 15. Influence of fabric anisotropy on the instability lines represented in the e-p' space for (a) $\alpha_{\sigma}=0^{\circ},\ b=0$ (b) $\alpha_{\sigma}=45^{\circ},\ b=0.5$ (c) $\alpha_{\sigma}=90^{\circ},\ b=1.5$

as α_{σ} increases; however, this trend is reverted for large Lode angles, i.e., $\theta=120^{\circ}$ to 240° . These trends are associated with the coupling between the Lode angle, α_{σ} , and the initial fabric direction (represented by the fabric tensor in Table 2). The trend of η_f decreasing as α_{σ} increases has been observed experimentally for Lode angles and initial fabric directions that are expected to be consistent with that in our simulations (i.e., the Fanni et al., 2022 study previously discussed). However, experimental studies considering interactions of α_{σ} , initial fabric, and a wide range of Lode angles, as considered in this study, are unavailable. Future experimental studies should inspect this further.

To further illustrate the anisotropy role (i.e., variations in α_σ and b=0) on η_f , Fig. 15 shows contours of instability points on a e-p' space. Each contour corresponds to a constant q value. Within a contour, it

can be observed that as e increases, the p' value at instability also increases, indicating a decrease in η_f . For increasing α_σ and b (Fig. 15 b,c), the instability contours shift towards the right, indicating that for a given e and q, instability occurs at a higher p', resulting in a lower η_f , consistent with previous discussions. These observations highlight again the role of fabric anisotropy on static liquefaction triggered by CSD loading.

4.4. Effect of initial soil fabric intensity F_{in}

In this section, we assess the effects of initial fabric intensity on the instability triggering and η_f under CSD loading by conducting numerical simulations considering different fabric intensities, following

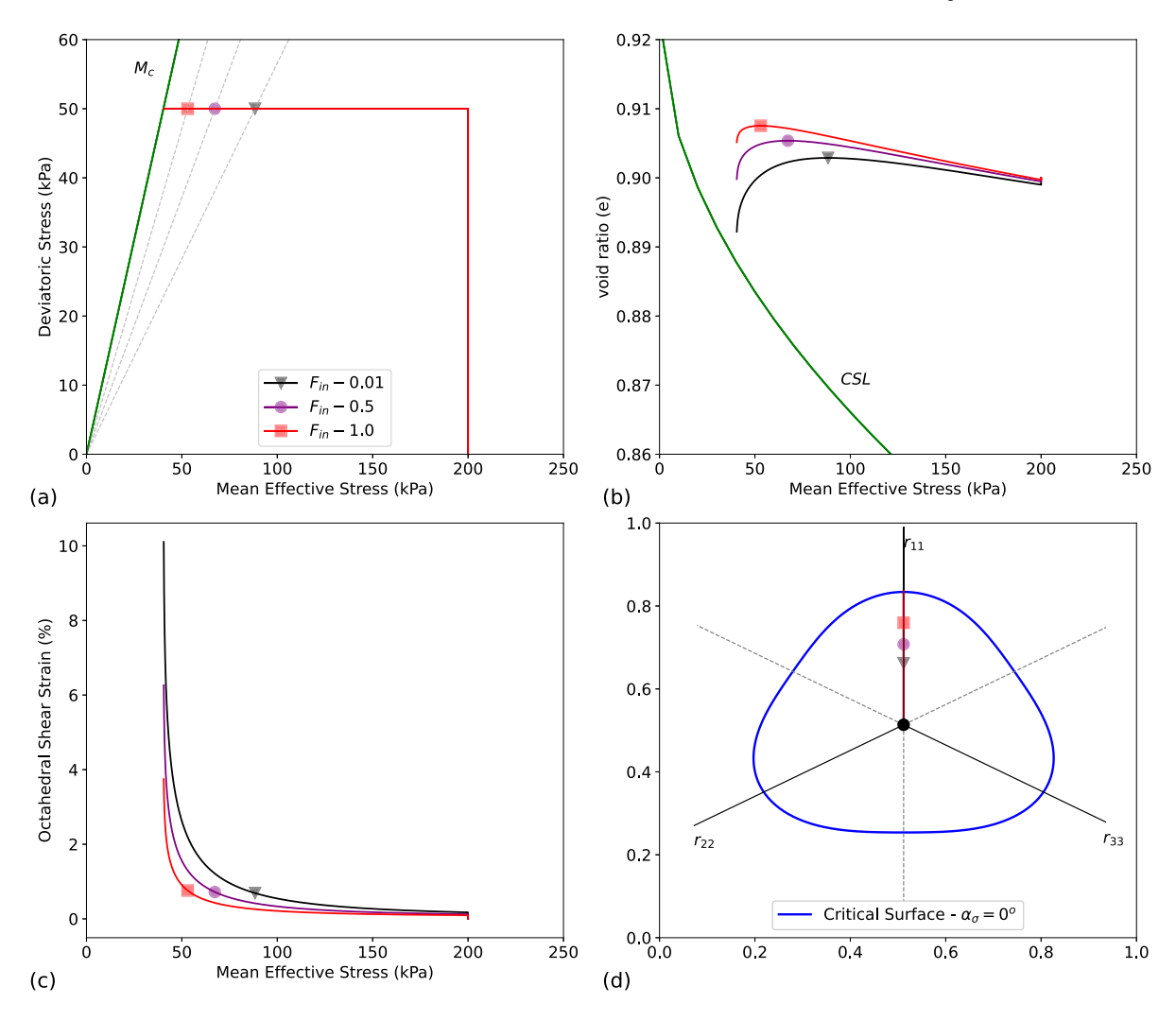


Fig. 16. SANISAND-F constitutive model responses for Firozkuh No. 161 sand specimen at $e_{in}=0.90$ and p'=200 kPa and different fabric intensities $F_{in}=[0.01,0.5,1.0]$ subjected to CSD loading path with $\theta=0^\circ$ and $\alpha_\sigma=0^\circ$ (a) Stress path (b) e-p' space (c) Octahedral shear strain Vs mean effective stress (d) Volumetric strain vs mean effective stress. The marker points represent the instability points.

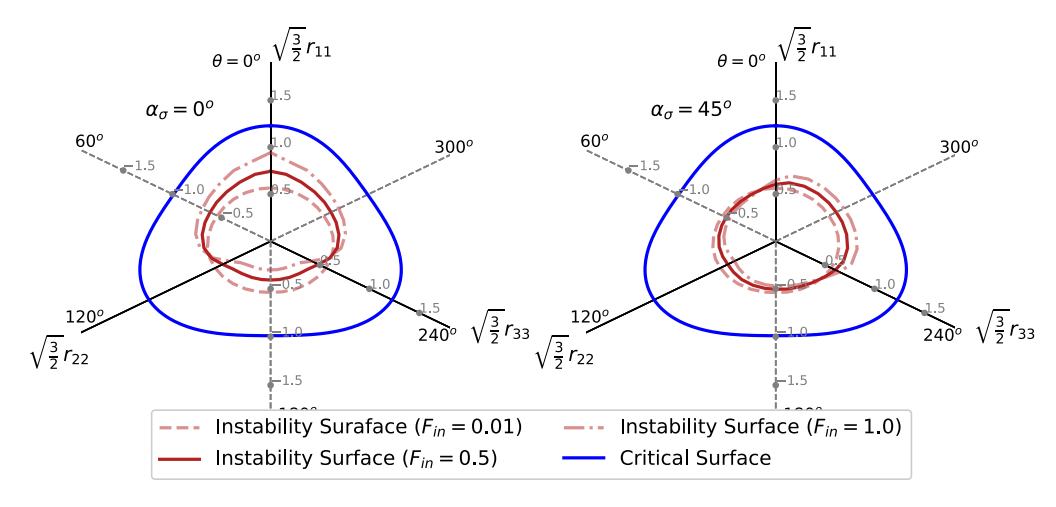


Fig. 17. Effect of initial fabric intensity on the instability surface obtained for various loading paths, θ varying from 0° to 360° with constant $\alpha_{\sigma} = 0^{\circ}$ and $\alpha_{\sigma} = 45^{\circ}$.

the structure for the fabric tensor in Table 2. In the simulations, we only change F_{in} and consider all other constitutive parameters fixed. Fig. 16 shows representative responses considering $\alpha_{\sigma}=0^{\circ}$, $\theta=0^{\circ}$, $e_{in}=0.9$,

 $p_{in}'=200$ kPa, a targeted q_{oct} of 50 kPa, and variable fabric intensities of $F_{in}=[0.01,0.5,1.0]$. $F_{in}=0.01$ represents an almost isotropic fabric, and $F_{in}=1.0$ represents a highly anisotropic fabric. It can be observed

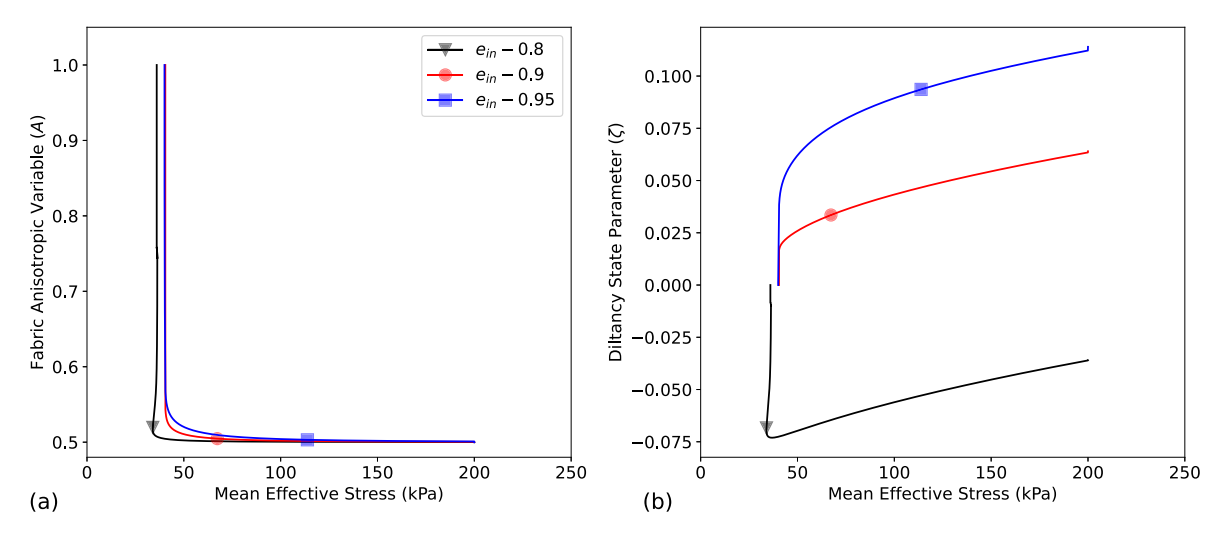


Fig. 18. Evolution of fabric variables for the SANISAND-F constitutive model simulations of Firoozkuh No. 161 sand specimen at p' = 200 kPa subjected to CSD loading path in triaxial compression conditions for different initial void ratios $e_{in} = [0.8, 0.9, 0.95]$ (a) Evolution of *A* (b) Evolution of *ζ*. The marker points represent the instability triggering points.

that as F_{in} increases, the initial volume increase during the stress relief of the CSD loading is enhanced (see Fig. 16b); hence, leading to a higher η_f (see Fig. 16a). This response is associated with the evolution of the fabric anisotropic variable (A=FN), which controls dilatancy. For instance, for $b{=}0$ and the considered cross-anisotropic fabric, the loading direction is aligned in the direction of fabric, implying N=1, and A=F. Larger F_{in} implies larger A, which in turn implies smaller dilatancy state parameter ζ (see Equation 4) and thus enhances the dilative response (see Equations 13 & 9). The evolution of shear strains is also consistent with the patterns observed in previous simulations. Lastly, the stress paths travel vertically upwards (as $\theta=0^\circ$) in the π -plane (see Fig. 16d) with instability points at different distances from the critical surface due to different initial fabric intensities.

Fig. 17 shows instability surfaces estimated for different F_{in} , α_{σ} of 0° and 45° , for the full range of Lode angles. Considering $\alpha_{\sigma} = 0^{\circ}$, it can be observed that for the isotropic fabric ($F_{in} = 0.01$), the instability surface is almost symmetric with respect to the origin. In contrast, the instability surface estimated for the anisotropic fabric ($F_{in} = 1.0$) is not symmetric and particularly distorted for $\theta = 0^{\circ}$ and $\theta = 180^{\circ}$, where η_f has its maximum and minimum values and also changes more significantly relative to the $F_{in} = 0.01$ instability surface. In the case of $\alpha_{\sigma} = 45^{\circ}$, a significant change in the instability surfaces and η_f relative to the $\alpha_\sigma=0^\circ$ cases can be observed. For instance, there is a significant decrease in η_f for cases with a high fabric intensity ($F_{in} = 1.0$) and Lode angles between 0° and 60° . Again, these changes are influenced by the coupling between the Lode angle, α_{σ} , and the initial fabric direction. As previously discussed, the only study we know of exploring α_{σ} effects under CSD loading is the Fanni et al. (2022) study, where the authors also considered different reconstitution procedures to represent different fabrics. They observed that dry-pluviated specimens showed a greater reduction in η_f when α_{σ} is increased for b values in the order of 0.2. Moreover, Yang et al. (2008) highlighted that both dry pluviation and moist tamping produce cross-anisotropic fabrics; however, the fabric anisotropy is higher for dry pluviation. Thus, our results (i.e., Figs. 16 and 17) are in qualitative agreement with the experimental observations by Fanni et al. (2022) and Yang et al. (2008).

5. Discussion

The instability criterion for type 1 instability (Eqs. (30) and (31)), which is the most relevant for practical applications as it is associated with initially loose states. The analytical equation for η_f is a function of constitutive model parameters, A, ζ (representing state), and β_{in} .

The constitutive model parameters, once calibrated, remain constant, and β_{in} is also constant as there is no stress reversal in a CSD stress path. In contrast, A and ζ evolve during the CSD loading. To illustrate this, Fig. 18 shows the evolution of internal fabric variables (A, ζ) for the simulation results highlighted in Fig. 8. It can be observed that the fabric anisotropy variable, A does not evolve significantly until the instability point considering both loose and dense samples. However, as the CSD loading progresses, A starts to increase exponentially with a slight change in p' (see Fig. 18a). The dilatancy state parameter (ζ), on the other hand, gradually decreases, approaching zero value as the loading progresses in the loose samples. In the dense case, the initial ζ is negative, initially decreasing, and then exponentially increasing towards 0. Overall, until the instability point, the evolution in A is not significant, and the evolution in ζ is only minor (see Fig. 18a and 18b). Thus, these features could be considered to relax the instability criterion previously derived and neglect the evolution of A and ζ in the estimation of η_f by using Eqs. (30) and (31). The benefit of this approach is that a numerical simulation of a particular CSD stress path would not be required anymore. Once the calibration of constitutive model parameters is conducted, and the anisotropy loading parameters are defined (i.e., Lode angle, α_{σ} , F_{ip}), η_f could be directly estimated from the state, i.e., e and p' just before the initiation of CSD loading. Here we assume that we know the soil's state just before the CSD loading initiation. Fig. 19 assesses the performance of this approach by comparing η_f values estimated numerically, analytically (i.e., by neglecting the evolution of A and ζ), and experimentally. Even though differences can be noticed between the numerical and analytical η_f , the estimates are reasonably close. In general, the numerical η_f is ≈ 1.1 times the analytical η_f . Thus, the analytical-based estimate is conservative for the constitutive model parameters considered in this study. This is appealing as it simplifies the η_f estimate, still being on the conservative side. Future studies should inspect this further by considering a broader set of materials and constitutive model parameters. Lastly, when assessing the initial fabric effects in this study, we only considered variations of F_{in} . It may be the case that other SANISAND-F constitutive parameters could be affected by changes in F_{in} (Li and Dafalias, 2012). However, we are not aware of experimental information to rigorously investigate this. Current efforts considering fabric measurements (Viggiani and Tengattini, 2019; Zhao et al., 2021) are expected to be instrumental in shedding light on this issue and should be considered in future research.

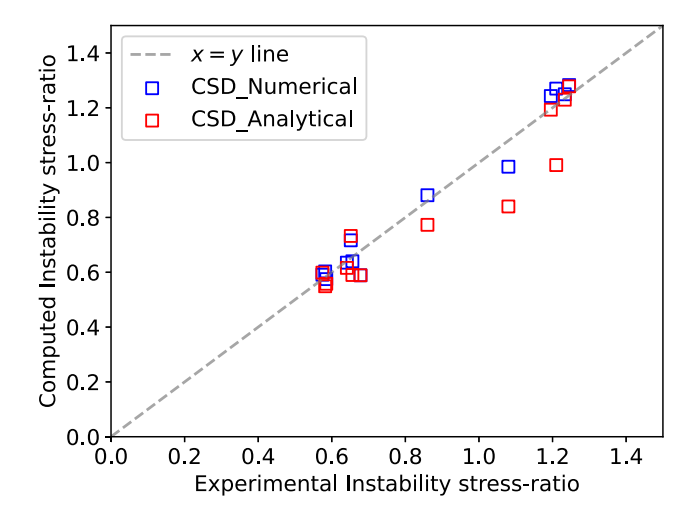


Fig. 19. Comparison of experimental instability stress-ratio against the computed instability stress ratio both by numerical and analytical methods for the Firoozkuh No. 161 sand and the Silica Fine Sand.

6. Conclusions

In this study, we have used the ACST framework to investigate the instability conditions under CSD stress paths, considering the role of fabric anisotropy, multiaxial loading, and state in a comprehensive manner, something that has not been addressed in previous efforts. CSD stress paths can be particularly important because the possibility of a water table increase is difficult to obviate during the lifetime of a slope system and because any predecessors of a potential failure would be minimal, as shown by several case history failures discussed in the introduction section of this study.

Towards the goals of our study, we first assessed the performance of the ACST-based SANISAND-F constitutive model under CSD stress paths, finding it satisfactory. Importantly, the adequate performance of the SANISAND-F model was assessed considering the same set of constitutive parameters under triaxial compression, triaxial extension, and CSD stress paths, showing the model's robustness. Moreover, subsequent numerical simulations showed that the instability onset of initially loose materials is governed by a trade-off between plastic and volumetric strains. Fabric effects were incorporated in defining different instability criteria. Specifically, instability stress ratios, which in a multiaxial space can be represented by the distance between the origin and instability surfaces in the π -plane, for initially loose and dense states were derived. Interestingly, the derived instability surfaces are fabric dependent and also depend on the loading conditions. Moreover, they are asymmetric relative to the π -plane axes, in contrast to what would be expected when fabric effects are not considered.

It was shown that the ACST framework, through the implementation of the SANISAND-F model, is able to provide valuable insights into assessing the relative effects of fabric (inherent and induced), α_{σ} , Lode angle, and state on the instability under CSD stress paths. Importantly, for conditions that are representative of the scarce experimental CSD information considering anisotropic effects, our numerical-based findings are consistent with the experimental counterparts. For example, instability is triggered regardless of the state of the soil (dense or loose). In addition, considering the cross-anisotropic fabrics used in this study, which resemble the initial fabric in experimental tests, η_f decreases as the Lode angle increase and α_{σ} increase for typical values used on experiments (i.e., α_{σ} between 0° to 90° , and Lode angles between 0° to 60°). Moreover, η_f increases as the initial fabric intensity (F_{in}) increases, and the decrease in η_f given a α_{σ} increase is more significant if F_{in} is higher (i.e., a more anisotropic fabric), consistent with the experimental Fanni et al. (2022) study. Importantly, our results also highlight the coupling between the Lode angle, α_{σ} , and F_{in} . For instance, when considering scenarios that have not been accounted for in previous experimental efforts, the onset of instability for a given Lode angle and an increasing α_{σ} can be promoted or not, depending on the interactions between the loading and fabric directions. Future experimental efforts considering broader ranges for Lode angle, α_{σ} , and F_{in} can provide additional insights in this direction. Last, we also found that relaxing the instability criterion (Eqs. (30) and (31)) by neglecting the evolution of A and ζ provides reasonable η_f estimates that are on the conservative side for the constitutive model parameters considered in this study. The benefit of this approach is that once the constitutive model parameters are calibrated and anisotropy loading parameters defined (i.e., Lode angle, α_{σ} , F_{in}), η_f can be directly estimated by using Eqs. (30) and (31), without conducting numerical simulations, which is appealing. This approach was appropriate for the set of constitutive model parameters considered in this study, but it should be inspected further in future studies considering a broader set of constitutive model parameters once more CSD experimental information comparable to the one used in this study becomes available.

CRediT authorship contribution statement

Srinivas Vivek Bokkisa: Methodology, Verification, Formal analysis, Data curation, Visualization, Writing – original draft, Writing – review & editing. **Jorge Macedo:** Conceptualization, Methodology, Resources, Writing – original draft, Project administration, Funding acquisition, Writing – review & editing. **Alexandros L. Petalas:** Conceptualization, Methodology, Software, Resources, Writing – original draft, Writing – review & editing.

Declaration of competing interest

The authors declare that they have no known competing financial interests or personal relationships that could have appeared to influence the work reported in this paper.

Data availability

Data will be made available on request.

Acknowledgments

This material is based upon work supported by the National Science Foundation (NSF) under the Grants No. CMMI 2013947 and 2145092. Any opinions, findings, conclusions, or recommendations expressed in this material are those of the author(s) and do not necessarily reflect the views of the National Science Foundation.

Appendix. Derivation of instability stress ratio β_f for Type-1 instability

The three constitutive ingredients in Eq. (28) are the elastic bulk modulus K_p , the dilatancy D and the plastic modulus K_p , which are defined based on the SANISAND-F model in Eqs. 5, 13 and 14 respectively. Substituting them in Eq. (28) and denoting β as β_f , the stress ratio at the onset of flow liquefaction, we get:

$$\frac{(M_{\theta}^{b} - \beta_{f})}{\beta_{f}(\beta_{f} - \beta_{in})(M_{\theta}^{d} - \beta_{f})} = \underbrace{\frac{2A_{d}(1 + \nu)(2.97 - e)^{2}}{3(1 - 2\nu)(1 + e)h_{1}exp(h_{2}A)(e^{-1} - c_{h})^{2}}}_{E}$$
(A.1)

After rearranging:

$$\beta_{f}^{3} - (\beta_{in} + M_{\theta}^{d})\beta_{f}^{2} - \left(\frac{1}{F_{e}} - \beta_{in}M_{\theta}^{d}\right)\beta_{f} + \frac{M_{\theta}^{b}}{F_{e}} = 0$$
(A.2)

Eq. (A.2) can be recast in a simple cubic polynomial form as shown below:

$$\beta_f^3 + C_1 \beta_f^2 + C_2 \beta_f + C_3 = 0 \tag{A.3}$$

with $C_1 = -\left(\beta_{in} + M_{\theta}^d(\zeta)\right)$, $C_2 = -\left(\frac{1}{F_e} - \beta_{in} M_{\theta}^d(\zeta)\right)$, and $C_3 = \frac{M_{\theta}^b(\zeta)}{F_e}$. As shown in Najma and Latifi (2017), the general cubic polynomial has three roots, of which two are imaginary and one is a real acceptable root. The real root can be estimated as Najma and Latifi (2017):

$$\beta_f = \frac{-C_1}{3} \left[1 + 2 \left(1 - 3 \frac{C_2}{C_1^2} \right)^{0.5} \cos \left(\frac{\phi + 4\pi}{3} \right) \right]$$

$$\phi = \cos^{-1} \frac{1 + \frac{27C_3}{2C_1^3} - \frac{9C_2}{2C_1^2}}{\left(1 - \frac{3C_2}{C^2} \right)}$$
(A.4)

At the initiation of flow liquefaction, the stress ratio β is equal to β_f .

References

- Alipour, M.J., Lashkari, A., 2018. Sand instability under constant shear drained stress path. Int. J. Solids Struct. 150, 66–82.
 Anderson, S.A., Riemer, M.F., 1995. Collapse of saturated soil due to reduction in
- confinement. J. Geotech. Eng. 121 (2), 216–220.

 Azizi A. 2009 Experimental Study and Modeling Behavior of Granular Materials in
- Azizi, A., 2009. Experimental Study and Modeling Behavior of Granular Materials in Constant Deviatoric Stress Loading. Amirkabir University of Technology, Iran.
- Azizi, A., Imam, R., Soroush, A., Zandian, R., 2009. Behavior of sands in constant deviatoric stress loading. Predict. Simul. Methods Geohazard Mitig. 319–324.
- Been, K., Jefferies, M.G., 1985. A state parameter for sands. Géotechnique 35 (2), 99–112.
- Bishop, A.W., Hutchinson, J.N., Penman, A.D.M., Evans, H.E., 1969. Geotechnical investigation into the causes and circumstances of the disaster of 21 October 1966. pp. 1–80, A selection of technical reports submitted to the Aberfan Tribunal HMSO.
- Bokkisa, S.V., Macedo, J., Petalas, A.L., Arson, C., 2022. Assessing static liquefaction triggering considering fabric anisotropy effects under the ACST framework. Comput. Geotech. 148, 104796. http://dx.doi.org/10.1016/j.compgeo.2022.104796, URL https://www.sciencedirect.com/science/article/pii/S0266352X22001537.
- Brand, E.W., 1981. Some thoughts on rain-induced slope failures. In: Proc. 10th ICSMFE, 1981, Vol. 3. pp. 373–376.
- Chu, J., Leong, W.K., Loke, W.L., Wanatowski, D., 2012. Instability of loose sand under drained conditions. J. Geotech. Geoenviron. Eng. 138 (2), 207–216.
- Chu, J., Leroueil, S., Leong, W.K., 2003. Unstable behaviour of sand and its implication for slope instability. Can. Geotech. J. 40 (5), 873–885.
- Chu, J., Wanatowski, D., Leong, W.K., Loke, W.L., He, J., 2015. Instability of dilative sand. Geotech. Res. 2 (1), 35–48.
- Dafalias, Y.F., Manzari, M.T., 2004. Simple plasticity sand model accounting for fabric change effects. J. Eng. Mech. 130 (6), 622–634.
- Darve, F., Flavigny, E., Meghachou, M., 1995. Yield surfaces and principle of superposition: Revisit through incrementally non-linear constitutive relations. Int. J. Plast. 11 (8), 927–948.
- Dong, Q., Xu, C., Cai, Y., Juang, H., Wang, J., Yang, Z., Gu, C., 2016. Drained instability in loose granular material. Int. J. Geomech. 16 (2), 4015043.
- Eckersley, D., 1990. Instrumented laboratory flowslides. Geotechnique 40 (3), 489–502.
 Embankments, D., Committee, S., 2021. Edenville and Sanford Dam Failures: Field Reconnaissance Report. American Society of Civil Engineers Reston. VA.
- Fanni, R., Reid, D., Fourie, A., 2022. Effect of principal stress direction on the instability of sand under the constant shear drained stress path. Géotechnique 1–54.
- Fotovvat, A., Sadrekarimi, A., Etezad, M., 2022. Instability of gold mine tailings subjected to undrained and drained unloading stress paths. Géotechnique 1–51.
- France, J.W., Alvi, I., Williams, J.L., Miller, A., Higinbotham, S., 2022. Investigation of failures of Edenville and Sanford dams. Independent forensic team final report. Retrieved from the website: https://damsafety.org/MI-Final-Report.
- Gajo, A., Piffer, L., De Polo, F., 2000. Analysis of certain factors affecting the unstable behaviour of saturated loose sand. Mech. Cohes.-Frictional Mater.: Int. J. Exp., Model. Comput. Mater. Struct. 5 (3), 215–237.
- Golchin, A., Lashkari, A., 2014. A critical state sand model with elastic-plastic coupling. Int. J. Solids Struct. 51 (15–16), 2807–2825.
- Harp, E.L., Wells, W.G., Sarmiento, J.G., 1990. Pore pressure response during failure in soils. Geol. Soc. America Bull. 102 (4), 428–438.
- Hill, R., 1958. A general theory of uniqueness and stability in elastic-plastic solids. J. Mech. Phys. Solids 6 (3), 236–249.
- Ishihara, K., 1996. Soil behaviour in earthquake geotechnics.
- Jefferies, M., Been, K., 2015. Soil Liquefaction: A Critical State Approach. CRC Press. Jefferies, M., Morgenstern, N.R., Van Zyl, D.J.A., Wates, J., 2019. Report on the NTSF Embankment Failure, Cadia Valley Operations for Ashurst Australia. Newcrest Mining Ltd, Melbourne, Australia, pp. 1–119.

- Konrad, J., 1993. Undrained response of loosely compacted sands during monotonic and cyclic compression tests. Géotechnique 43 (1), 69–89.
- Kramer, S.L., 1985. Liquefaction of Sands Due to Non-Seismic Loading (Landslide, Triaxial, Compliance, Montana). University of California, Berkeley.
- Kramer, S.L., 1996. Geotechnical Earthquake Engineering. Pearson Education India.
- Lade, P.V., 1992. Static instability and liquefaction of loose fine sandy slopes. J. Geotech. Eng. 118 (1), 51–71.
- Lashkari, A., Karimi, A., Fakharian, K., Kaviani-Hamedani, F., 2017. Prediction of undrained behavior of isotropically and anisotropically consolidated Firoozkuh sand: Instability and flow liquefaction. Int. J. Geomech. 17 (10), 4017083.
- Lashkari, A., Khodadadi, M., Binesh, S.M., Rahman, M.M., 2019. Instability of particulate assemblies under constant shear drained stress path: DEM approach. Int. J. Geomech. 19 (6), 4019049.
- Li, X.S., Dafalias, Y.F., 2002. Constitutive modeling of inherently anisotropic sand behavior. J. Geotech. Geoenviron. Eng. 128 (10), 868–880.
- Li, X.S., Dafalias, Y.F., 2012. Anisotropic critical state theory: Role of fabric. J. Eng. Mech. 138 (3), 263–275.
- Lindenberg, J., Koning, H.L., 1981. Critical density of sand. Geotechnique 31 (2), 231-245.
- Manzari, M.T., Dafalias, Y.F., 1997. A critical state two-surface plasticity model for sands. Geotechnique 47 (2), 255–272.
- Morgenstern, N.R., 2001. Geotechnics and mine waste management–update. In: Seminar on Safe Tailings Dam Constructions. pp. 54–67.
- Morgenstern, N.R., Vick, S.G., Viotti, C.B., Watts, B.D., 2016. Report on the immediate causes of the failure of the Fundão Dam. Fundão Tailings Dam Rey, Panel.
- Najma, A., Latifi, M., 2017. Analytical definition of collapse surface in multiaxial space as a criterion for flow liquefaction occurrence. Comput. Geotech. 90, 120–132.
- Niemunis, A., Grandas-Tavera, C.E., 2017. Computer aided calibration, benchmarking and check-up of constitutive models for soils. Some conclusions for neohypoplasticity. In: Holistic Simulation of Geotechnical Installation Processes. Springer, pp. 168–192.
- Nocilla, A., Coop, M.R., Colleselli, F., 2006. The mechanics of an Italian silt: An example of 'transitional'behaviour. Géotechnique 56 (4), 261–271.
- Olson, S.M., 2000. 1907 Static liquefaction flow failure on the north dike or Wachusett dam, J. Geotech, Geoenviron, Eng.,
- Petalas, A.L., Dafalias, Y.F., Papadimitriou, A.G., 2020. SANISAND-F: Sand constitutive model with evolving fabric anisotropy. Int. J. Solids Struct. 188–189, 12–31. http://dx.doi.org/10.1016/j.ijsolstr.2019.09.005.
- Pradhan, T.B.S., Tatsuoka, F., Horii, N., 1988. Simple shear testing on sand in a torsional shear apparatus. Soils Found. 28 (2), 95–112.
- Ramos, A.M., Andrade, J.E., Lizcano, A., 2012. Modelling diffuse instabilities in sands under drained conditions. Géotechnique 62 (6), 471–478.
- Reid, D., Fourie, A., Ayala, J.L., Dickinson, S., Ochoa-Cornejo, F., Fanni, R., Garfias, J., Da Fonseca, A.V., Ghafghazi, M., Ovalle, C., 2021a. Results of a critical state line testing round robin programme. Géotechnique 71 (7), 616–630.
- Reid, D., Fourie, A., Fanni, R., Vulpe, C., Haliday, A., 2021b. Some considerations when using deformation monitoring to manage the static liquefaction risks of TSFs. In: Online Conference ANCOLD 2021, Australia.
- Robertson, P.K., de Melo, L., Williams, D.J., Wilson, G.W., 2019. Report of the expert panel on the technical causes of the failure of Feijão dam I. Retrieved from the website: http://www.b1technicalinvestigation.com/.
- Rudnicki, J.W., Rice, J., 1975. Conditions for the localization of deformation in pressure-sensitive dilatant materials. J. Mech. Phys. Solids 23 (6), 371–394.
- Sadrekarimi, A., 2014. Effect of the mode of shear on static liquefaction analysis. J. Geotech. Geoenviron. Eng. 140 (12), 04014069.
- Sasitharan, S., Robertson, P.K., Sego, D., Morgenstern, N.R., 1993. Collapse behavior of sand. Can. Geotech. J. 30 (4), 569–577.
- Sawicki, A., Świdziński, W., 2010a. Modelling the pre-failure instabilities of sand. Comput. Geotech. 37 (6), 781–788.
- Sawicki, A., Świdziński, W., 2010b. Stress-strain relations for dry and saturated sands. Part I: Incremental model. J. Theoret. Appl. Mech. 48, 309–328.
- Sawicki, A., Świdziński, W., 2010c. Stress-strain relations for dry and saturated sands. Part II: Predictions. J. Theoret. Appl. Mech. 48 (2), 329–343.
- Sayao, A., Vaid, Y.P., 1996. Effect of intermediate principal stress on the deformation response of sand. Can. Geotech. J. 33 (5), 822–828.
- Shibuya, S., 1985. Undrained behaviour of granular materials under principal stress rotation.
- Sibille, L., Nicot, F., Donze, F.V., Darve, F., 2007. Material instability in granular assemblies from fundamentally different models. Int. J. Numer. Anal. Methods Geomech. 31 (3), 457–481.
- Skopek, P., Morgenstern, N.R., Robertson, P., Sego, D.C., 1994. Collapse of dry sand. Can. Geotech. J. 31 (6), 1008–1014.
- Sun, W., 2013. A unified method to predict diffuse and localized instabilities in sands. Geomech. Geoeng. 8 (2), 65–75.
- Viggiani, G., Tengattini, A., 2019. Recent developments in laboratory testing of geomaterials with emphasis on imaging. In: Proceedings of the XVII ECSMGE-2019 Reykjavík, Iceland, Vol. 9. p. 2019.
- Vilhar, G., Jovičić, V., Coop, M.R., 2013. The role of particle breakage in the mechanics of a non-plastic silty sand. Soils Found. 53 (1), 91-104.

- Wanatowski, D., 2005. Strain Softening and Instability of Sand Under Plane-Strain Conditions (Ph.D. thesis). Nanyang Technological University, School of Civil and Environmental Engineering.
- Wanatowski, D., Chu, J., 2007. Static liquefaction of sand in plane strain. Can. Geotech. J. 44 (3), 299–313.
- Wanatowski, D., Chu, J., 2012. Factors affecting pre-failure instability of sand under plane-strain conditions. Géotechnique 62 (2), 121–135.
- Wanatowski, D., Chu, J., Loke, W.L., 2010. Drained instability of sand in plane strain. Can. Geotech. J. 47 (4), 400–412.
- Wu, Q.X., Xu, T.T., Yang, Z.X., 2020. Diffuse instability of granular material under various drainage conditions: Discrete element simulation and constitutive modeling. Acta Geotech. 15 (7), 1763–1778.
- Yang, J., Li, X.S., 2004. State-dependent strength of sands from the perspective of unified modeling. J. Geotech. Geoenviron. Eng. 130 (2), 186–198.
- Yang, Z.X., Lit, X.S., Yang, J., 2008. Quantifying and modelling fabric anisotropy of granular soils. Geotechnique 58 (4), 237–248. http://dx.doi.org/10.1680/geot. 2008.58.4.237.
- Yoshimine, M., Özay, R., Sezen, A., Ansal, A., 1999. Undrained plane strain shear tests on saturated sand using a hollow cylinder torsional shear apparatus. Soils Found. 39 (2), 131–136.
- Zhao, C.-F., Pinzón, G., Wiebicke, M., Andò, E., Kruyt, N.P., Viggiani, G., 2021.
 Evolution of fabric anisotropy of granular soils: X-ray tomography measurements and theoretical modelling. Comput. Geotech. 133, 104046.